scientific **data**

DATA DESCRIPTOR

Check for updates

MCI GPP: ensembling a global model- and climate-independent gross primary productivity for 2001–2023

Jiabin Pu [1], Yuhe Chang[1], Si Gao[2], Shanning Bao[3], Kai Yan [2✉], Xian Sun[4], Nuno Carvalhais [5] & Ranga B. Myneni[1]

Gross primary productivity (GPP), the starting point of carbon entry into the land, is crucial for understanding the global carbon cycle. Previous research have debated incorporating the CO_2 fertilization effect (CFE) and canopy structural traits into GPP modeling. This study systematically evaluates their influence, demonstrating that CFE improves GPP estimation accuracy and significantly alters long-term trends. Interestingly, a two-leaf model (TLM) achieved comparable accuracy to the production efficiency model (PEM). Leveraging these insights, we generated 12 distinct GPP datasets and integrated them into a novel model- and climate-independent (MCI) GPP product using random forest regression and spatio-temporal tensor models. The MCI GPP estimates average global GPP from 2001 to 2023 at 141.9 ± 4.0 Pg C yr^{-1}, with a significant global increase of 5.7 Pg C yr^{-1} per decade. Validation against AmeriFlux data shows MCI GPP outperforms other global products (MOD17, GOSIF, X-Base Fluxcom), achieving an R^2 of 0.72 and RMSE of 1.86 g C m^{-2} d^{-1}. Available on Zenodo, this robust 0.05° monthly dataset provides a valuable resource for carbon-climate feedback studies.

Background & Summary

Since the early 1980s, a period concurrent with a surge in global population from 4.5 to 8 billion and an expansion of global GDP from 11 to 100 trillion USD, atmospheric CO_2 concentrations have markedly increased from approximately 340 ppm to over 420 ppm. This rise is principally driven by anthropogenic emissions from fossil fuel combustion[1]. The elevated CO_2 levels are strongly implicated in driving ongoing climate change[2], which has, in turn, altered plant phenology and precipitated structural and functional shifts within terrestrial ecosystems[3]. These shifts encompass modifications in canopy dynamics, species distributions, and ecological integrity across diverse biomes[4–6]. Gross primary productivity (GPP), quantified as the total carbon assimilated by vegetation via photosynthesis per unit time, represents a cornerstone metric of ecosystem function. It fundamentally underpins the terrestrial carbon balance and serves as a crucial indicator of biogeochemical cycles[3,7,8]. Nevertheless, significant uncertainties persist in global GPP estimations; reported annual values exhibit considerable variation, ranging from almost 100 to 150 Pg C yr^{-1}, depending on the methodology employed[9–11]. These discrepancies stem from inherent limitations in model parameterization, inconsistencies within input data, and methodological challenges in scaling localized observations to global estimates[11–14].

Over the past decades, eddy covariance (EC) flux towers have provided foundational high-precision benchmarks for regional GPP estimates via direct measurements of canopy CO_2 exchange[15,16]. The FluxNet initiative[17], a global network spanning major biomes, provides standardized, quality-controlled datasets that facilitate cross-site analyses of carbon flux dynamics. Leveraging these EC observations, various upscaling algorithms, including machine learning (ML) methods, have been utilized with gridded satellite and climate

[1]Department of Earth and Environment, Boston University, Boston, MA, 02215, USA. [2]State Key Laboratory of Remote Sensing and Digital Earth, Advanced Interdisciplinary Institute of Satellite Applications, Faculty of Geographical Science, Beijing Normal University, Beijing, 100875, China. [3]National Space Science Center, Chinese Academy of Sciences, Beijing, 100190, China. [4]Aerospace Information Research Institute, Chinese Academy of Sciences, Beijing, 100094, China. [5]Department for Biogeochemical Integration, Max-Planck-Institute for Biogeochemistry, 07745, Jena, Germany. ✉e-mail: kaiyan@bnu.edu.cn

datasets to extrapolate tower-based GPP estimates to global scales[13,18,19]. Nonetheless, the spatial distribution of EC flux towers remains sparse and geographically biased, resulting in significant underrepresentation in critical regions such as tropical forests and high-latitude ecosystems[20]. This uneven coverage introduces considerable uncertainty when scaling tower-derived GPP globally, particularly in heterogeneous landscapes where vegetation-climate interactions exhibit non-linear responses[13]. Furthermore, the 'black-box' nature of many ML algorithms renders them susceptible to overfitting or underfitting climate factors; this limitation is exemplified by the low sensitivity of the Fluxcom GPP product to changes in atmospheric CO_2 concentration, revealing structural deficiencies in simulating long-term trends[21].

Satellite remote sensing (RS) has emerged as the pre-eminent tool for quantifying GPP, offering unparalleled capabilities for spatially continuous monitoring and seamless global coverage that effectively circumvent the limitations inherent in ground-based observational networks. Global GPP estimation relies on several distinct satellite-derived approaches. One approach leverages Solar-induced chlorophyll fluorescence (SIF) products (e.g., from OCO-2, TROPOMI), which provide a direct proxy for photosynthetic activity, facilitating data-driven GPP estimation through empirical SIF-GPP relationships across biomes[22,23]. Alternatively, light use efficiency (LUE) models, conceptually rooted in the Monteith framework[24], calculate GPP as the product of absorbed photosynthetically active radiation (APAR) and a LUE coefficient; prominent operational examples include the MODIS/VIIRS[25–27], GLASS[28,29], and VPM[30] GPP products. Furthermore, process-based models simulate GPP by mechanistically coupling carbon, water, and energy cycles[31], exemplified by models such as the P-model[32], BESS[33], and BEPS[34]. Among these methodologies, LUE models have gained the most widespread adoption for global GPP assessments, despite their empirical relationship, largely owing to their relative simplicity, parsimonious parameter requirements, and operational efficiency[35].

However, earlier upscaled LUE GPP datasets, exemplified by the MODIS GPP product, generally neglected the direct physiological effects of rising atmospheric CO_2 on leaf biochemistry and the influence of vegetation canopy architecture[25]. Increasing atmospheric CO_2, recognized as a key driver behind at least half of the enhanced land carbon sink observed over recent decades, directly stimulates leaf-level photosynthetic rates, leading to increased net carbon assimilation and often promoting leaf area expansion[4,36]. Furthermore, elevated CO_2 is expected to reduce stomatal conductance, thereby increasing water use efficiency and potentially enhancing photosynthesis under water-limited conditions[37,38]. Consequently, these GPP products tend to underestimate long-term global GPP trends[5,39]. Additionally, conventional LUE models typically adopted a simplified 'big-leaf' representation (akin to production efficiency models (PEM)), failing to consider the radiation difference between sunlit and shaded leaves. However, canopy GPP is significantly related to horizontal canopy structure, particularly the difference between sunlit and shaded leaves in terms of photosynthetic capacity[40]. Sunlit leaves absorb both direct and diffuse radiation and can readily reach light saturation under high irradiance, whereas shaded leaves intercept primarily diffuse radiation, operating at light intensities often between the light compensation and saturation points[41–43]. Critically, neither contemporary PEM nor two leaf model (TLM) approaches fully capture the canopy's dynamic radiative configuration under diverse sky conditions, introducing uncertainty into GPP simulations from both model types[44]. PEM overlooks photosynthetic capacity differences between sunlit and shaded fractions, while TLM approaches have shown systematic underestimation of *in-situ* GPP under overcast and cloudy conditions[40,45]. Although recent advancements in LUE modelling, such as the EC-LUE and revised EC-LUE models, incorporate representations of CO_2 response and canopy structure and demonstrate improved simulation of long-term GPP changes globally[29,46], the precise quantification of CO_2 fertilization and canopy structural effects within the global GPP estimation framework remains challenging. Inadequate accounting for these factors continues to introduce substantial uncertainties into global GPP assessments.

To address the aforementioned problems and generate a set of long-term GPP products that consider these factors, this study plans to: 1) Integrate CFE and canopy structure stepwise in the MOD17 algorithmic framework and quantitatively assess the effects of both on GPP estimation; 2) Generate 12 set of GPP datasets based on the PEM and TLM frameworks with CFE module, combining MODIS GPP model and other LUE models, and forced by multi-source climate data; 3) Utilize FluxNet GPPs as baseline for training a random forest (RF) algorithm to establish the nonlinear relationship between the multi-model output and the measured GPP and subsequently generate a model- and climate-independent (MCI) GPP product; 4) Filtered high uncertainty pixels and employed an advanced gap-filling algorithm for missing value interpolation to guarantee data spatiotemporal continuity; 5) Conduct a systematic accuracy verification of the generated GPP products based on FluxNet-independent EC GPP and satellite-derived GPPs across multiple scales.

Methods

Input data. This study utilized three types of data for distinct purposes: (1) input data for MCI GPP estimation, (2) *in-situ* observations for model optimization and validation, and (3) existing GPP products for evaluation.

Input dataset for MCI GPP estimation. Two reanalysis climate datasets, GMAO MERRA-2 (https://gmao.gsfc.nasa.gov/reanalysis/MERRA-2), and ECMWF ERA-5 (https://cds.climate.copernicus.eu/cdsapp#!/dataset/reanalysis-era5-single-levels), were used to derive PEM and TLM, respectively. Core climate variables, including air temperature, dew point temperature, and incoming shortwave radiation, were extracted from these datasets as model inputs. Vapor pressure deficit (VPD) was subsequently calculated using air temperature and dew point temperature[47]. Additionally, several other climatic variables (net radiation, evapotranspiration, and precipitation) were obtained from the GLDAS NOAH-2.1 product (https://disc.gsfc.nasa.gov/datasets?keywords=GLDAS). Critical vegetation input parameters for PEM and TLM, fraction of absorbed photosynthetically active radiation (FPAR), and leaf area index (LAI), were acquired from the sensor-independent (SI) LAI/FPAR dataset[48]. All climate and vegetation data were harmonized to 0.05° spatial resolution. Atmospheric CO_2
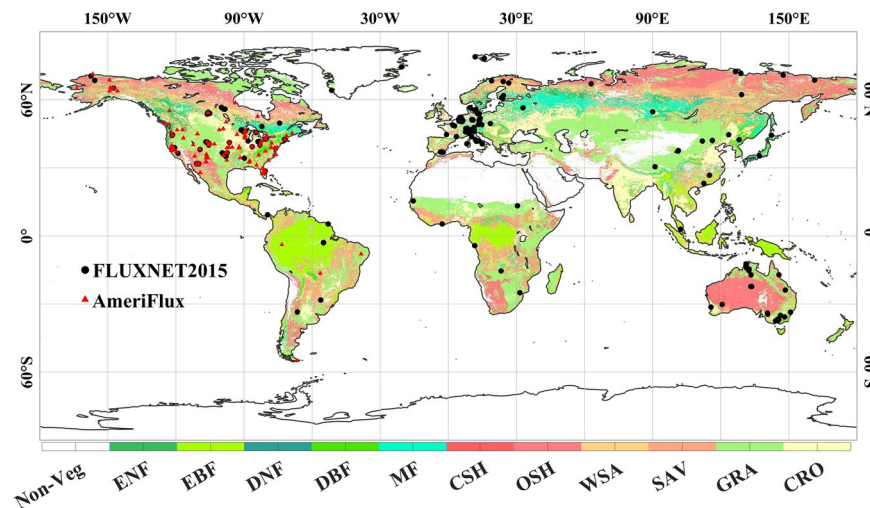
Fig. 1 Global distribution of FluxNet2015 (optimization) and AmeriFlux (validation) flux tower sites. The background shows MODIS land cover in 2020. Abbreviations: ENF (evergreen needleleaf forest), EBF (evergreen broadleaf forest), DNF (deciduous needleleaf forest), DBF (deciduous broadleaf forest), MF (mixed forest), CSH (closed shrubland), OSH (open shrubland), WSA (woody savanna), SAV (savanna), GRA (grassland), CRO (cropland).

concentrations, necessary for modeling the CFE[49], were sourced from NOAA daily records (https://gml.noaa. gov/ccgg/trends/).

Model parameterization utilized plant functional type (PFT) information derived from the MODIS MCD12Q1 product[50], which followed the UMD classification scheme (Fig. 1). This scheme aggregated vegetation types into 11 biome types: evergreen needleleaf forest (ENF), evergreen broadleaf forest (EBF), deciduous needleleaf forest (DNF), deciduous broadleaf forest (DBF), mixed forest (MF), closed shrubland (CSH), open shrubland (OSH), wooded savanna (WSA), savanna (SAV), grassland (GRA), and cropland (CRO).

In-situ data for optimization and validation. Monthly EC GPP measurements, covering the period 2001–2022, were sourced from the FluxNet2015[17] and AmeriFlux FluxNet[51] datasets. To enhance simulation accuracy, model parameters were optimized through constrained calibration using FluxNet2015 data (Table S1). While independent validation relied on *in-situ* GPP measurements from the AmeriFlux network (Table S3), which is distinct from FluxNet2015. As GPP cannot be directly measured at flux sites, it is typically derived by partitioning net ecosystem exchange (NEE). This study employed monthly GPP data derived from the nighttime partitioning method, retaining only high-quality observations (NEE_VUT_REF_QC > 0.8) for each year, ultimately yielding data from 193 sites (9548 monthly values) for optimization and 142 sites (7163 monthly values) for validation (Fig. 1).

Peer GPP products for evaluation. For intercomparison at site and global scales, performance was evaluated against several major GPP satellite products, encompassing LUE-based, SIF-based, and ML-based datasets. These included: (1) the MODIS GPP product, generated using MODIS FPAR and an LUE model sensitive to air temperature and VPD[25]; (2) the GOSIF GPP product, derived from biome-specific relationships between reconstructed SIF (based on discrete OCO-2 SIF soundings, remote sensing data from the MODIS, and meteorological reanalysis data) and tower GPP[22]; and (3) the X-Base Fluxcom GPP product, resulting from ML-based upscaling integrating flux tower estimates, remote sensing, and meteorological data[18]. All datasets were harmonized to a 0.05° spatial resolution and monthly temporal scale, applying a common mask for vegetated land areas[50]. The intercomparison period was constrained to 2001–2021, corresponding to the availability of the X-Base Fluxcom product.

Assessing the contribution of CFE and contrasting PEM with TLM. To evaluate the contribution of the CFE and distinguish between the PEM and TLM, this study designed three GPP configurations based on the original MODIS GPP algorithm: (1) PEM without CFE: the original MODIS GPP algorithm; (2) PEM with CFE: the original algorithm augmented by incorporating relative CFE; (3) TLM with CFE: a modified algorithm accounting for sunlit and shaded leaf separation and CFE integration. The contribution of CFE was quantified by comparing configurations 1 and 2. Differences between configurations 2 and 3 served to elucidate the distinctions between PEM and TLM frameworks. For these configurations, climate data from GMAO MERRA-2 and SI LAI/ FPAR were used as inputs, and model parameters were optimized using FluxNet2015.

Configuration 1, MODIS GPP is driven by FPAR, PAR, temperature, and VPD, which generate GPP $(g\,C\,m^{-2}\,d^{-1})$ as follows:

$$GPP_{PEM\ without\ CFE} = LUE_{opt} \times PAR \times FPAR \times f_{TMIN} \times f_{VPD}, \qquad (1)$$

where, LUE_{opt} is the optimal LUE (g C MJ^{-1}); PAR is the incident photosynthetically active radiation (MJ m^{-2} d^{-1}); FPAR is the fraction of vegetation absorbed PAR; f_{TMIN}^{M1} (Eq. 2) and f_{VPD}^{M1} (Eq. 3) are the temperature (daily minimum) and water stress scalar[25].

Configuration 2 is the model of PEM with CFE proposed by Yuan *et al.*[5], which generates GPP (g C m^{-2} d^{-1}) by the MODIS GPP program is modified to include the CFE as follows:

$$GPP_{PEM\ with\ CFE} = LUE_{opt} \times PAR \times FPAR \times f_{TMIN} \times f_{VPD} \times f(CO_2), \tag{2}$$

$$f(CO_2) = \frac{C_s^t}{C_s^{2001}}, \tag{3}$$

where $f(CO_2)$ is the effect of atmospheric CO_2 concentration on the GPP of configuration 1, which is the relative value of the current year C_s[28] compared to year 2001[5].

The TLM framework explicitly accounts for canopy structural heterogeneity by partitioning vegetation into sunlit and shaded leaves. Configuration 3, TLM with CFE calculated GPP as follows:

$$GPP_{TLM\ with\ CFE} = (LUE_{opt}^{sun} \times APAR_{sun} + LUE_{opt}^{shade} \times APAR_{shade}) \times f_{TMIN} \times f_{VPD} \times f(CO_2), \tag{4}$$

where LUE_{opt}^{sun} and LUE_{opt}^{shade} are the optimal LUE of sunlit and shaded leaves for TLM, respectively. $APAR_{sun}$ and $APAR_{shade}$ are the APAR of sunlit and shaded leaves, respectively. A detailed description of the models can be found in Supplement A.

Generation of MCI GPP. This study generated 12 sets of GPP by integrating the PEM and TLM frameworks with the MOD17 (incorporating CFE), EC-LUE, and MPI-Jena models, driven by meteorological forcings from GMAO MERRA-2 and ECMWF ERA5. Utilizing FLUXNET2015 as a baseline, the RF algorithm was applied to establish nonlinear relationships between these model outputs and measured GPP, thereby producing robust, model- and climate-independent GPP products. To ensure data reliability and continuity, rigorous quality control was applied to filter out pixels with high uncertainty, and then an advanced gap-filling algorithm was employed to interpolate missing values (See the flow chart in Fig. 2).

Generating 12 GPPs based on diverse models and climate variables. This study utilized configuration 2 'PEM with CFE' (Eq. 2) and configuration 3 'TLM with CFE' (Eq. 4) as PEM1 and TLM1, respectively. Each of these was driven by GMAO MERRA-2 (C1) and ECMWF ERA5 (C2), resulting in four sets of GPPs. The other two LUE models previously mentioned, EC-LUE and MPI-Jena, were processed similarly to generate eight sets of GPPs. Detailed descriptions of all six model implementations (the three models applied within both PEM and TLM frameworks) can be found in Supplement A. Brief descriptions of the EC-LUE and MPI-Jena models are provided below.

The EC-LUE model dynamically regulates LUE based on observed canopy-scale VPD and soil moisture constraints derived from FluxNet sites[28,29,46]. Thus, the PEM2 and TLM2 calculated GPP as follows:

$$GPP_{PEM2} = LUE_{opt}^{PEM2} \times PAR \times FPAR \times min(f_T^{M2}, f_{VPD}^{M2}) \times C_s, \tag{5}$$

$$GPP_{TLM2} = (LUE_{opt}^{TLM2,sun} \times APAR_{sun} + LUE_{opt}^{TLM2,shade} \times APAR_{shade}) \times min(f_T^{M2}, f_{VPD}^{M2}) \times C_s, \tag{6}$$

where LUE_{opt}^{PEM2} is the optimal LUE (gC MJ^{-1}) for PEM2; $LUE_{opt}^{TLM2,sun}$ and $LUE_{opt}^{TLM2,shade}$ are the optimal LUE of sunlit and shaded leaves for TLM2; f_T^{M2} and f_{VPD}^{M2} are the temperature and water stress scalars, respectively.

The MPI-Jena model[43,52] evaluates GPP for PEM3 and TLM3 as:

$$GPP_{PEM3} = LUE_{opt}^{PEM3} \times PAR \times FPAR \times f_T^{M3} \times f_{VPD,CO_2}^{M3} \times f_W^{M3} \times f_L^{M3} \times f_{CI}^{M3}, \tag{7}$$

$$GPP_{TLM3} = (LUE_{opt}^{TLM3,sun} \times APAR_{sun} \times f_L^{TLM3,sun} + LUE_{opt}^{TLM1,shade} \times APAR_{shade} \times f_L^{TLM3,shade})$$
$$\times f_T^{M3} \times f_{VPD,CO_2}^{M3} \times f_W^{M3} \times f_{CI}^{M3}, \tag{8}$$

where LUE_{opt}^{PEM3} is the optimal LUE (g C MJ^{-1}) for PEM3; $LUE_{opt}^{TLM3,sun}$ and $LUE_{opt}^{TLM3,shade}$ are the optimal LUE of sunlit and shaded leaves for TLM3; f_T^{M3} is the temperature stress scalar for PEM3/TLM3; f_{VPD,CO_2}^{M3} is the water stress scalar that consider CFE for PEM3/TLM3[53]; f_W^{M3}, f_L^{M3}, and f_{CI}^{M3} are soil moisture (W), light saturation effect (L), and cloudiness index (CI) effects on PEM3/TLM3 GPPs, respectively. $f_L^{TLM3,sun}$ and $f_L^{TLM3,shade}$ are the f_L^{M3} for sunlit and shaded leaves, respectively.

It is important to note that this step was performed at a daily resolution (2001–2023) to generate 12 GPP time series. However, all subsequent steps operated at a monthly resolution, where the daily-scale GPPs were aggregated into monthly values.
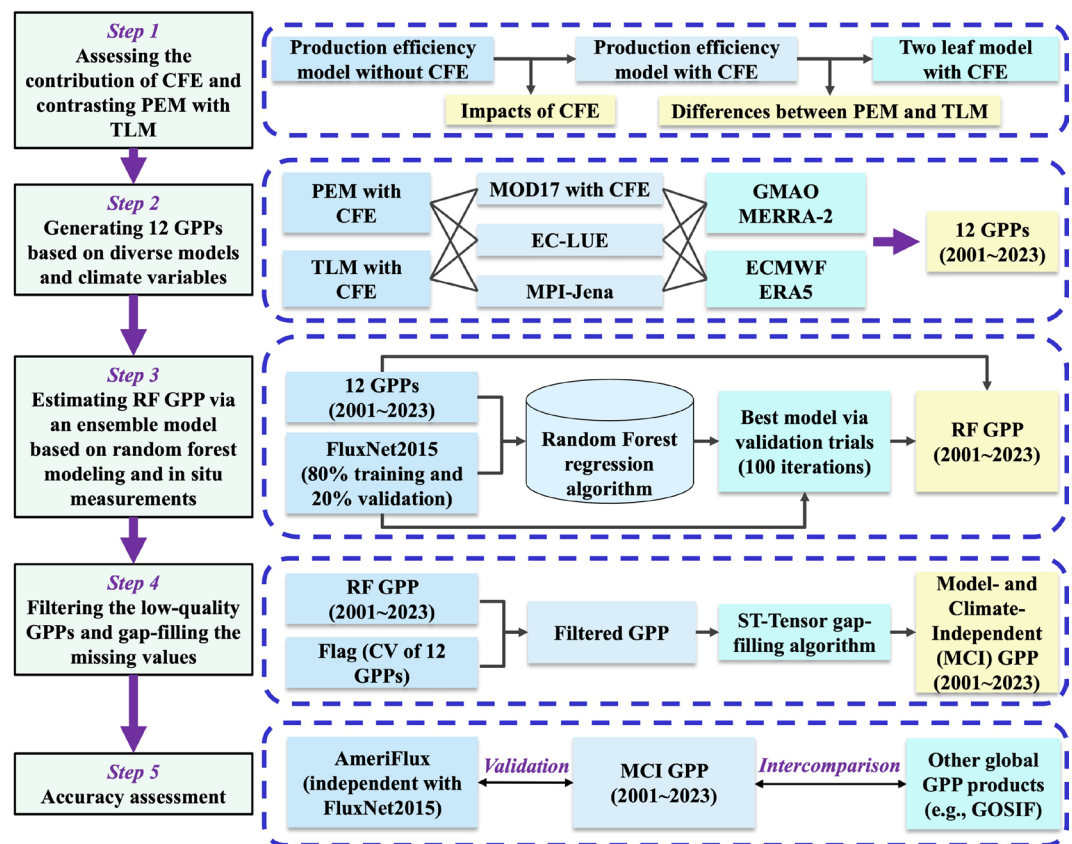
Fig. 2 Schematic diagram of the generation of model- and climate-independent (MCI) GPP. Here the 'MOD17 with CFE', 'EC-LUE', and 'MPI-Jena' are three light use efficiency models used; 'GMAO MERRA-2' and 'ECMWF ERA5' are two independent climate datasets; 'FluxNet2015' and 'AmeriFlux' are two site-level datasets for optimization, training, and validation. CFE: CO_2 fertilization effect; PEM: production efficiency model; TLM: two leaf model; RF: random forest; ST-Tensor: spatio-temporal tensor.

Estimating RF GPP via an ensemble model based on RF modelling and in-situ measurements. Consistent with previous research indicating that ensemble models generally provide more accurate estimates across global regions compared to individual models[54,55], this study leveraged the RF model to mitigate the inherent uncertainties associated with single-model GPP estimations. The RF algorithm was employed to discern the relationships between the 12 simulated GPP datasets and *in situ* GPP observations from FluxNet2015. This approach aimed to generate a consolidated GPP product exhibiting enhanced robustness and reduced dependence on specific model structures or climate forcing datasets. The RF method achieves this by aggregating predictions from numerous decision trees, implicitly optimizing input contributions based on learned feature importance. Specifically, the RF regression model was implemented using MATLAB's 'TreeBagger' function with carefully optimized hyperparameters: 120 decision trees to balance computational efficiency and ensemble stability, and a minimum leaf size of 15 samples to prevent overfitting, utilizing parallel computing for acceleration. Input features included the twelve GPP datasets, latitude, land cover type, and month of the year. The target variable was the tower-based GPP from the FluxNet2015 dataset. Using a stratified 80/20 split, 80% of the data was allocated for model training and 20% for validation, with the root mean square error (RMSE) serving as the primary performance metric. Through 100 bootstrap iterations, the optimal model configuration demonstrating the minimal validation RMSE was systematically identified. The coefficient of determination (R^2) and RMSE for this optimal model at each FluxNet2015 site are detailed in Table S1. The resulting RF model effectively synthesized the twelve input GPP datasets while incorporating spatial (latitude, land cover) and temporal (monthly cycle) information, generating a globally consistent monthly GPP product at 0.05° resolution spanning the period 2001–2023. This ensemble approach inherently reduces dependencies on specific climate datasets and mitigates single-model biases through nonlinear feature learning, and the rigorous training-validation protocol ensures the robustness of the final product.

Filtering the low-quality GPPs and gap-filling the missing values. Despite the generation of the RF GPP product, a significant limitation arises from the substantial inherent uncertainties within the 12 input GPP datasets. These uncertainties, stemming from inter-model variability in representing climate change responses and discrepancies between climate forcing data, propagate into the final GPP estimates. To address this challenge, this study implemented a two-step approach involving quality filtering and gap filling. First, GPP inputs associated with high uncertainty were identified and filtered out. Second, a spatial-temporal tensor (ST-Tensor) completion

model, based on established methodologies[48,56,57], was applied to reconstruct missing values in the remaining data, aiming for a more accurate and spatiotemporally consistent GPP estimation. The specific steps were executed as follows:

1) Filtering low-quality GPPs. Spatiotemporal uncertainty within the GPP ensemble was quantified using the coefficient of variation (CV), calculated as the ratio of the standard deviation to the mean value across the twelve input GPPs for each pixel and time step. This normalized metric accounts for proportional variability, enabling meaningful comparisons across different ecosystems. A conservative CV threshold of 50% was applied to ensure data reliability. Pixels where the CV exceeded 50% were assigned a quality flag of 0, and their corresponding RF GPP values were removed. Conversely, pixels with a CV of 50% or less were flagged as 1, and their RF GPP values were retained for the next step.

2) Tensor rearrangement. While standard tensor representations effectively capture local spatial similarity and short-term temporal relationships, they may not explicitly represent important periodic patterns (e.g., seasonal cycles). Therefore, data restructuring was performed before tensor completion. For each pixel, the one-dimensional multi-year time series was reshaped into a two-dimensional matrix, where columns represent individual years and rows represent months within those years. Concurrently, the two-dimensional spatial grid was transformed into a one-dimensional vector indexing the pixels. This data rearrangement process is illustrated by the following equation:

$$X_{m \star m \star T} \rightarrow Y_{m^2 \star ny \star nm},$$ (9)

where X is the original tensor, Y is the transformed tensor, m denotes the spatial length of the original tensor, and T denotes the total number of observations in the entire time series, which is equal to the number of years (ny) multiplied by the number of months in a year (nm).

3) Iteration weight update and gap-fill. The rearranged third-order tensor, structured along spatial, intra-annual (monthly), and inter-annual (yearly) dimensions, is amenable to analysis based on its underlying low-rank structure. The tensor rank, reflecting the correlations and structural redundancy across these dimensions, is key to the fidelity of gap filling. A lower tensor rank indicates greater internal coherence within the data, which enables the reliable estimation and imputation of missing values (where Flag = 0) by leveraging the patterns present in the observed data across all modes. This effective rank is linked to the ranks of the matrices resulting from unfolding the tensor along each mode. Therefore, the gap-filling process in this study is formulated as an optimization problem and aims to find a completed, low-rank tensor that accurately reconstructs the observed data points (where Flag = 1), as represented by the following equation designed to solve this optimization task:

$$\min \sum_{i=1}^{3} w_n \times \mathrm{rank}(Y_n),$$ (10)

where w_n is the weight corresponding to Y_n that is always non-negative and satisfies $\sum_{i=1}^{3} w_n = 1$. To solve Eq. (10), the process begins by iteratively determining the weights of the three mode matrices. Initialized equally ($w_1 = w_2 = w_3 = 1/3$), these weights are updated using the singular value decomposition-based method from[57]. With optimized weights, Eq. (10) is efficiently solved via the algorithm of[58], which employs a logarithmic operator. This operator improves tensor rank approximation, enhancing estimation accuracy[59].

4) Iterate L1 trend filtering. Following the ST-Tensor completion process, the reconstructed GPP time series may still contain residual noise due to uncertainties in the Flag data. To address this, an iterative L1 trend filtering method[57,60] is applied, which denoises 1D time series by balancing residual regularization and smoothing. Let y represent the noisy series and z the filtered output. The method optimizes a trade-off between two competing goals: (a) fidelity to the observed data and (b) smoothness of the filtered output. This is achieved by optimizing the following objective function (Eq. 11):

$$Q = 0.5 \times \| y - z \|_2^2 + \lambda \| D_z \|_1,$$ (11)

where D_z represents the second-order difference matrix and λ is the regularization parameter that balances the fidelity and smoothness terms. In practice, this method excels at preserving turning point details due to its L1 regularization. After ST-Tensor completion, residual noise is assumed to exhibit negative bias. Initial iterations apply the L1 trend filter to smooth the GPP time series, replacing only noisy values while retaining high-quality data. Subsequent iterations fully replace all flagged noise. Through repetition, this balances noise suppression with data fidelity, yielding a final output that is both gap-free and noise-free.

5) Reshape the tensor. Following the reverse process of rearrangement in step 2), the filled and filtered GPP tensor is returned to its original form. All steps done, the MCI GPP was generated.

Evaluations of the MCI GPP. The MCI GPP will first be evaluated for its accuracy at the local scale through comparison with data from the AmeriFlux estimates[51]. These reference AmeriFlux (Table S3) are distinct from the FluxNet2015 data previously employed for parameterizing the LUE variable within the three PEMs and three TLMs. Initially, the accuracy of the temporal GPP will be assessed using the R^2 and RMSE per site (Table S3). Subsequently, the spatiotemporal variability of MCI GPP will be validated against GPP observations across all sites. Finally, the performance of MCI GPP was compared against other peer GPP datasets.

At the large scale, two metrics will be used to quantify the inherent uncertainty of the global MCI GPP. And the interannual GPP trends of the MCI GPP were then evaluated against three other published global-scale independent GPP data sets. In addition, a newly proposed framework[61] for assessing the physical consistency between two terrestrial products was used in this study to examine the temporal consistency between MCI GPP and other global GPP products.

Uncertainty metrics. The MCI GPP product is generated through a two-step process: initial retrieval via the RF algorithm, followed by gap-filling using the ST-Tensor method for pixels with high standard deviation. To evaluate the quality of this hybrid product, we use two key metrics: the standard deviation of the 12 GPPs (StdGPP) and the retrieval index (RI). The StdGPP metric reports the response differences to various models and climate variables, serving as a measure of solution accuracy at the pixel level. However, this metric is only calculated when the RF-based retrieval uncertainty is below 50% (as described in Section "Generation of MCI GPP"). Consequently, StdGPP cannot be calculated for pixels that are subsequently gap-filled by the ST-Tensor method, as these pixels lack the 12 original GPP inputs. Therefore, we use the RI (see Eq. 12) as an essential, complementary quality metric. RI characterizes the proportion of pixels successfully retrieved by the high-quality, RF-based algorithm, effectively serving as a measure of the overall regional or global quality. In summary, a reliable assessment of the MCI GPP product quality requires the combination of both metrics: StdGPP provides a granular, pixel-by-pixel quality measure for the RF-retrieved data, while RI offers an aggregate measure of overall retrieval success for the product.

$$\text{RI} = \frac{\text{N. of pixels retrieved by the RF algorithm}}{\text{N. of pixels retrieved by the RF algorithm} + \text{N. of pixels gap filled by the ST} - \text{Tensor method}}, \quad (12)$$

Trends analysis. Trends in annual average GPPs were evaluated by the Mann–Kendall (MK) test in this study. The MK test is a non-parametric statistical test commonly used for climate diagnostics and prediction. It enables the detection of monotonic trends in time series data, helping to determine if significant trends exist[62]. The MK test is employed as follows:

$$S = \sum_{i=1}^{n-1} \sum_{j=i+1}^{n} \text{sgn}(x_j - x_i), \quad (13)$$

$$\text{Var}(S) = \frac{n(n-1)(2n+5) - \sum_{i=1}^{m} t_i(t_i - 1)(2t_i + 5)}{18}, \quad (14)$$

$$Z_s = \begin{cases} \dfrac{S-1}{\sqrt{\text{Var}(S)}}, & \text{if } S > 0 \\ 0, & \text{if } S = 0 \\ \dfrac{S+1}{\sqrt{\text{Var}(S)}}, & \text{if } S < 0 \end{cases} \quad (15)$$

Equation 13 calculates the sum (S) of step function values, which represents the differences between values at different points (x_j and x_i) in the time series. The variables n and m denote the number of data points and the number of tied groups (recurring data sets), respectively. Next in Eq. 14, the variance (Var(S)) is calculated by assessing the magnitude of S to evaluate the statistical significance of the detected trends. Where the t_i is the number of the ties (the number of repeats in the extent i). Finally, this study calculated the test statistic Z_s (Eq. 15). When $|Z_s| > Z_{1-\alpha/2}$, the null hypothesis (i.e., no trend) is rejected and the α is a special significance level. Here, this study used the significance level of $\alpha = 0.1$ and the $Z_{1-\alpha/2} = 1.28$. Thus, the trends with P-value ≤ 0.1 were statistically significant in this paper.

Consistency assessment framework. To analyze the level of agreement between simultaneous GPP changes, it is first necessary to assess the significance of each change using uncertainty to determine the confidence level (C_f) of the change from one GPP to the next. The C_f is determined by the ratio between the overlap region and the full range of values between two consecutive GPPs and their uncertainties. The full range is the interval of values that may exist between GPPs when uncertainty is taken into account to determine the maximum and minimum ranges, and the overlap range represents only the common value between the two intervals and indicates the degree of similarity between the observations. If the change is large but the relevant ranges (value ± uncertainty) do not overlap, a confidence level of 100% in the change is indicated[61]. This study quantified spatial uncertainty using the 5 × 5 neighborhood sliding window method, where the standard deviation of each pixel point is calculated. This local standard deviation matrix can effectively characterize spatial heterogeneity, with regions of high values corresponding to locations where spatial fluctuations are significant (e.g., edges or anomalies), and regions of low values reflecting a homogeneous and stable spatial structure. If there is an overlap between the observed value of the change and its uncertainty, this highlights the degree of similarity and therefore a lower level of confidence in the change.

The ratio between the overlap and the full range of values determines the confidence in the change: the greater the overlap, the less important the change. Therefore, the C_f is given as:

$$C_f \big|_t^{t+1} = 100 \times \left(1 - \frac{O_l}{f_l}\right), \frac{O_l}{f_l} \in [0,1],$$ (16)

where O_l is the range of variation overlap, given by the following equation:

$$O_l = \begin{cases} (v_{t+1} + u_{t+1}) - (v_t + u_t), v_{t+1} < v_t \\ (v_t + u_t) - (v_{t+1} - u_{t+1}), v_{t+1} > v_t \end{cases},$$ (17)

and f_l the entire range is given by the following equation:

$$f_l = \begin{cases} (v_t + u_t) - (v_{t+1} - u_{t+1}), v_{t+1} < v_t \\ (v_{t+1} + u_{t+1}) - (v_t - u_t), v_{t+1} > v_t \end{cases},$$ (18)

where v is the GPP and u is the uncertainty associated with successive observations at t and t+1.

All changes in GPP were analyzed and categorized based on the type of change that occurred simultaneously. Three possible classifications of changes were considered: (1) increasing, (2) decreasing, or (3) no confidence in the change. To be classified as an increasing or decreasing change, the C_f value had to be at least 50% higher. Otherwise, it was classified as no significant change. Overall, nine possible combinations of categorizations can occur when considering simultaneous changes in GPPs. This confusion matrix was used to derive consistency and deviation metrics. Physical consistency (the definition can be found in Table S4) can take three forms: (1) n_{33}: GPP increases significantly at the same time; (2) n_{11}: a simultaneous significant decrease in GPP; 3) n_{22}: a change in GPP that is simultaneously categorized as insignificant at a low confidence level. All other combinations were considered inconsistent. Based on this confusion matrix, overall agreement (OA) was determined by the total percentage of coherent simultaneous changes, given by:

$$OA = \frac{\sum_{i=1}^3 n_{ii}}{N}$$ (19)

where n_{ii} is the number of cases that fell into each coherent change classification type (i = 1, 2, 3) and N is the total number of considered cases.

Data Records

The global gridded 0.05° MCI GPP is generated and validated at daily scale from 2001 to 2023. Then the monthly and annual scale GPP are aggregated based on daily scale, the evaluation parts were token at annual scale. The monthly MCI GPP is available at: https://doi.org/10.5281/zenodo.15204660[63]. The data type is double, and the unit is g C m^{-2} month^{-1}. The files were named as "MCI_GPP_ WGS84_0.05degree_Month_YYYYMM.tif " and stored in the GeoTiff format, where YYYY represents year, and MM represents month (e.g. MCI_GPP_ WGS84_0.05degree_Month _200101.tif).

Over the period from 2001 to 2023, the mean annual global MCI GPP across vegetated areas amounted to 141.9 ± 4.0 Pg C yr^{-1}. High-productivity regions (>3,000 g C m^{-2} yr^{-1}) are predominantly concentrated in tropical ecosystems, including the Amazon Basin, Congo Basin, and Southeast Asia (Fig. 3a-1). Subtropical zones, such as southeastern North and South America, exhibit moderate GPP levels (around 2,000 g C m^{-2} yr^{-1}). A substantial fraction (67.8%) of the global vegetated area displays relatively low productivity (0–1,600 g C m^{-2} yr^{-1}), primarily corresponding to boreal and arid/semi-arid ecosystems. Partitioning by vegetation type reveals that global GPP is dominated by evergreen broadleaf forests (EBF: 37.2 Pg C yr^{-1}), savannas (SAV: 25.9 Pg C yr^{-1}) and grasslands (GRA: 22.9 Pg C yr^{-1}), collectively account for over 50% of the total terrestrial productivity (Fig. 3a-2). Woody savannas (WSA: 17.6 Pg C yr^{-1}) and croplands (CRO: 15.8 Pg C yr^{-1}) provide the next largest contributions. Moderate inputs derive from mixed forests (MF: 6.6 Pg C yr^{-1}), open shrublands (OSH: 5.3 Pg C yr^{-1}), deciduous broadleaf forests (DBF: 4.6 Pg C yr^{-1}), and evergreen needleleaf forests (ENF: 3.2 Pg C yr^{-1}), while closed shrublands (CSH: 0.5 Pg C yr^{-1}) and deciduous needleleaf forests (DNF: 0.4 Pg C yr^{-1}) contribute minimally.

The long-term trends of GPP from 2001 to 2023 were determined with a linear regression analysis per pixel (Fig. 3b). Statistically significant positive trends were detected across 47.6% of the global vegetated area (totaling 106 million km^2). Regions exhibiting pronounced greening include Malaysia, Southeast Asia, the Indian Peninsula, Central Africa, northern and southeastern South America, and Central Europe (Fig. 3b-1). Conversely, declining GPP trends were observed in only 4.3% of global vegetated lands, primarily located in the Brazilian Amazon and Central Asia. Global GPP trends vary substantially by ecosystem type. Notably, ecosystems characterized by sparser vegetation—specifically savannas, grasslands, croplands, and shrublands (WSA, SAV, GRA, CRO)—account for over 75% of the total observed GPP increase (Fig. 3b-2). Although forests remain the dominant contributor to Earth's total plant productivity, their rate of GPP increase appears to be stabilizing globally, contributing only a marginal increment of 0.7 Pg C yr^{-1} decade^{-1} to the overall trend. Overall, satellite observations confirm the pronounced global greening trend reported since the early 2000s, characterized by terrestrial productivity increasing at approximately 3% per decade[64,65]. Our MCI GPP data corroborate this trend, indicating a global increase in carbon uptake equivalent to 5.7 Pg C yr^{-1} decade^{-1} during over the period 2001–2023 (Fig. 3b).
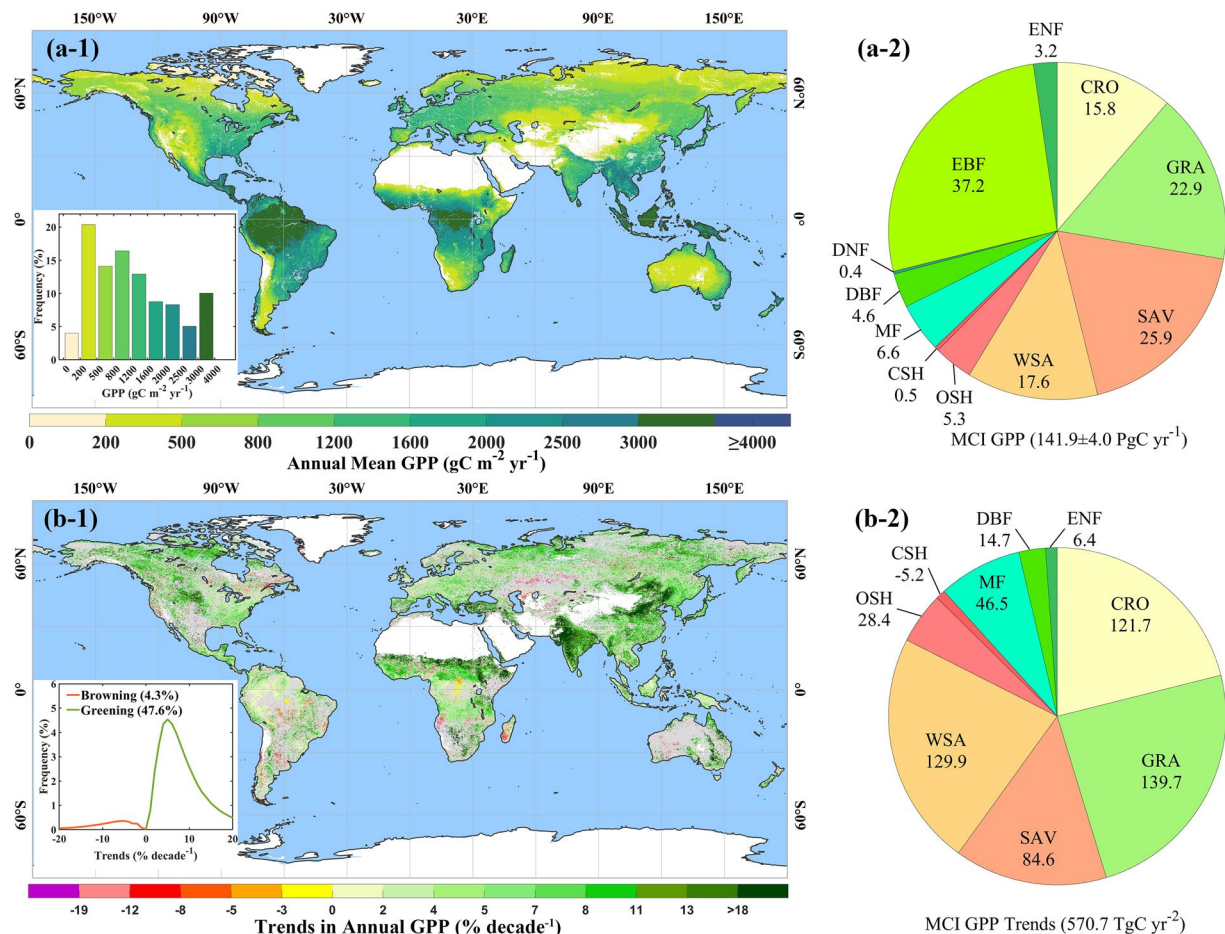
Fig. 3 Observed changes in MCI GPP during 2001–2023. (**a-1**) GPP averaged over the 23-year study period. The inset shows the histogram of multi-year average GPP. (**a-2**) Mean annual totals of GPP from 2001 to 2023 for different vegetation types over the globe. (**b-1**) Spatial pattern of statistically significant trends in MCI GPP. Only statistically significant trends are color-coded (Mann-Kendall test, P ≤ 0.1). The insets show the distribution of pixels exhibiting statistically significant trends. (**b-2**) Totals of annual GPP trends from 2001 to 2023 for different vegetation types across the globe.

Technical Validation

The contribution of CFE and contrasting PEM with TLM. Prior to incorporating the CFE modification, the PEM explained 57% ($R^2 = 0.57$) of the observed monthly variation in GPP across global EC monitoring sites (Fig. 4a). The integration of CFE significantly enhanced model performance (Fig. 4b): the R^2 increased to 0.62, while the RMSE decreased by nearly 10%, from 2.67 to 2.41 g C m^{-2} d^{-1}. Crucially, the CFE modification corrected a persistent underestimation bias in PEM; the average bias improved markedly from -0.74 g C m^{-2} d^{-1} to -0.06 g C m^{-2} d^{-1}, and the regression slope, indicating alignment between modeled and observed GPP, strengthened from 0.57 to 0.67. When evaluated against the FluxNet2015 benchmark GPP data, the TLM, incorporating CFE, exhibited similar overall accuracy to the CFE-enhanced PEM but demonstrated superior explanatory power, accounting for 63% of monthly GPP variability ($R^2 = 0.63$; Fig. 4c). Both the 'PEM with CFE' and the 'TLM with CFE' achieved an identical RMSE of 2.41 g C m^{-2} d^{-1}. However, TLM produced systematically higher GPP estimates; its bias shifted from slightly negative (-0.06 g C m^{-2} d^{-1} for the enhanced PEM) to near-neutral (0.02 g C m^{-2} d^{-1} for TLM), and its regression slope improved further to 0.73, suggesting stronger statistical agreement with observational data than the enhanced PEM. Nevertheless, a comparison of Fig. 4b,c indicates that TLM is prone to generating some abnormally high GPP estimates.

The incorporation of CFE significantly enhanced GPP magnitude across approx. 85.2% of global land areas (Fig. 5a, △GPP < 0 g C m^{-2} yr^{-1}). Within these regions, 25.8% exhibited significant GPP growth (△GPP < −240 g C m^{-2} yr^{-1}) in agricultural zones in China, India, and Sub-Saharan Africa. The decline in GPP after considering CFE is concentrated in the Amazon forest and sub-Saharan evergreen broadleaf forest (EBF) regions. Although elevated CO_2 levels typically enhance plant productivity, the CFE adjustment incorporates climatic feedback mechanisms, such as temperature and precipitation effects, which account for localized declines in moisture-limited or heat-stressed ecosystems. A direct comparison between 'TLM with CFE' and 'PEM with CFE' (Fig. 5b) indicated that while both models captured similar global patterns, they exhibited regional divergences: 53.1% of areas showed significantly higher GPPs (△GPP < 0 g C m^{-2} yr^{-1}) in 'TLM with CFE', and
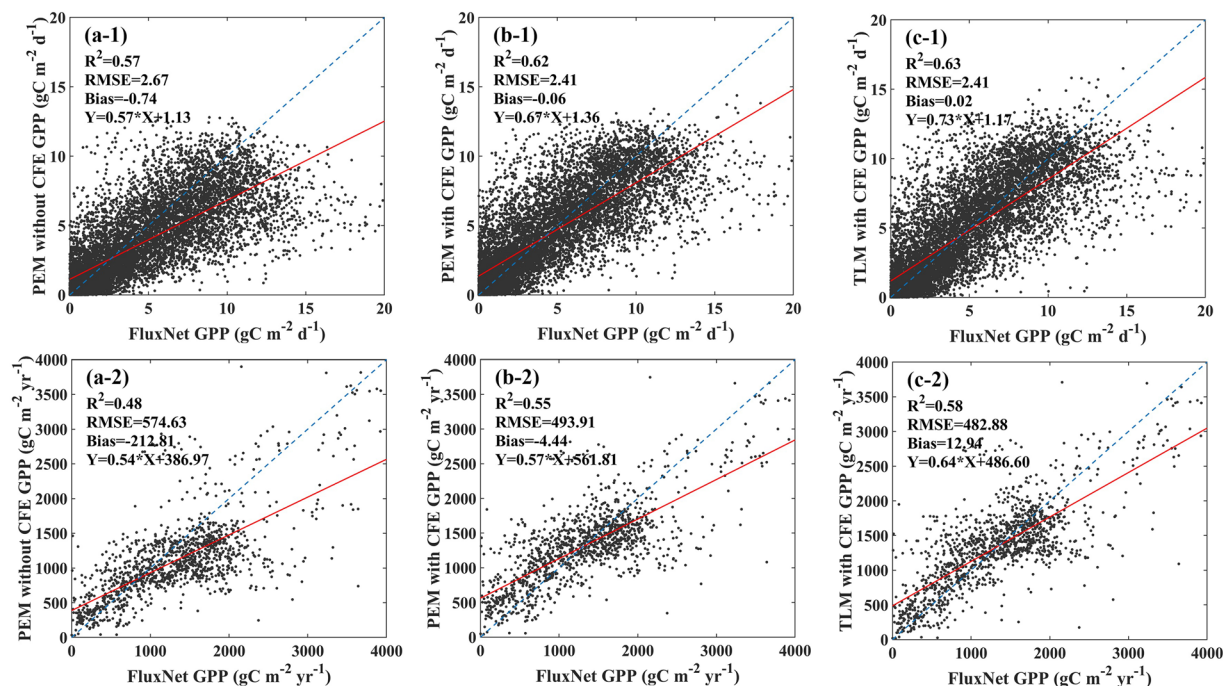
Fig. 4 Comparison of annual GPP from (**a**) PEM without CFE, (**b**) PEM with CFE, and (**c**) TLM with CFE with observations-based GPP from the FluxNet2015. The top 3 panels are daily scale GPP (g C m^{-2} d^{-1}) and the bottom 3 panels are annual GPP sum (g C m^{-2} yr^{-1}).

46.9% showed lower GPPs (ΔGPP > 0 g C m^{-2} yr^{-1}) compared to 'PEM with CFE'. These findings underscore the necessity of including CFE for accurate global GPP estimation and indicate that while 'PEM with CFE' and 'TLM with CFE' provide comparable GPP estimates overall, they retain distinct regional characteristics and predictive behaviors.

This study further evaluated model performance using the GOSIF GPP product as a reference dataset to quantify the impact of the CFE modification and assess differences between the PEM and TLM models. Results confirm that incorporating CFE markedly reduces systematic underestimation in global GPP estimates; PEM and TLM exhibited nearly identical performance levels after CFE adjustment. Without CFE, 35.5% of the global land area exhibited annual GPP values at least 160 g C m^{-2} yr^{-1} lower than GOSIF benchmarks (Fig. S1a). Following CFE implementation, this extent of underestimation was substantially reduced to 20.4% (Fig. S1b). The refined 'PEM with CFE' shows close agreement with GOSIF, with 73.0% of land areas exhibiting annual GPP differences within $\pm$ 320 g C m^{-2} yr^{-1} (Fig. S1b). 'TLM with CFE' performed comparably, with 72.1% of land areas falling within this same difference range (Fig. S1c).

Generation of 12 PEM/TLM GPPs, RF GPP, and MCI GPP. Within the MCI GPP estimation process, this study generated an ensemble of twelve GPP estimates using the PEM and TLM frameworks, incorporating three distinct LUE models (M1, M2, M3) and two meteorological climate datasets (C1, C2). Global annual GPP from these individual simulations ranged from 118.8 to 146.8 Pg C yr^{-1} (Table 1), with variations primarily observed in absolute magnitude rather than spatial patterns. All twelve GPP estimates exhibited consistent spatial distributions (Fig. S2); tropical ecosystems, particularly the Amazon Basin, Congo Basin, and Southeast Asia, consistently emerged as high-productivity regions, whereas over half of the global vegetated areas, including boreal and arid ecosystems, displayed low productivity. GPP estimates derived from PEM and TLM showed similar interannual variability (Fig. 6), although TLM generally yielded higher values than PEM. Furthermore, simulations driven by climate dataset C1 were largely consistent with those using C2. Among the LUE models, M3 produced the largest GPP magnitudes, followed by M1 and M2.

The most pronounced divergence across the GPP estimates occurred in their decadal trends, which ranged from 1.6 to 8.6 Pg C yr^{-1} decade^{-1}, while relative trends spanned 1.2% to 5.9% decade^{-1} (Table 1 and Fig. 6). Spatially, these discrepancies (Fig. S3) reflect model-specific responses to climate forcing data, differing both across models using the same climate input and within the same model under different climate datasets. Regionally, GPP in the Amazon Basin declined significantly in simulations employing M1C1, M2C1, and M2C2 configurations, irrespective of the framework (PEM or TLM), whereas other configurations showed only sporadic declines. In sub-Saharan Africa, decreasing trends were specific to the M1C2 and M2C2 simulations. Conversely, regions exhibiting significant GPP increases displayed spatially consistent patterns across all model configurations, differing primarily in trend magnitude.

Both PEM and TLM GPP outputs were subsequently optimized using FluxNet2015 data, and their post-optimization performance was evaluated. Optimized PEM configurations achieved R^2 values ranging from 0.56 to 0.62 and RMSE values below 2.58 g C m^{-2} d^{-1} (Fig. S4). Optimized TLM configurations showed
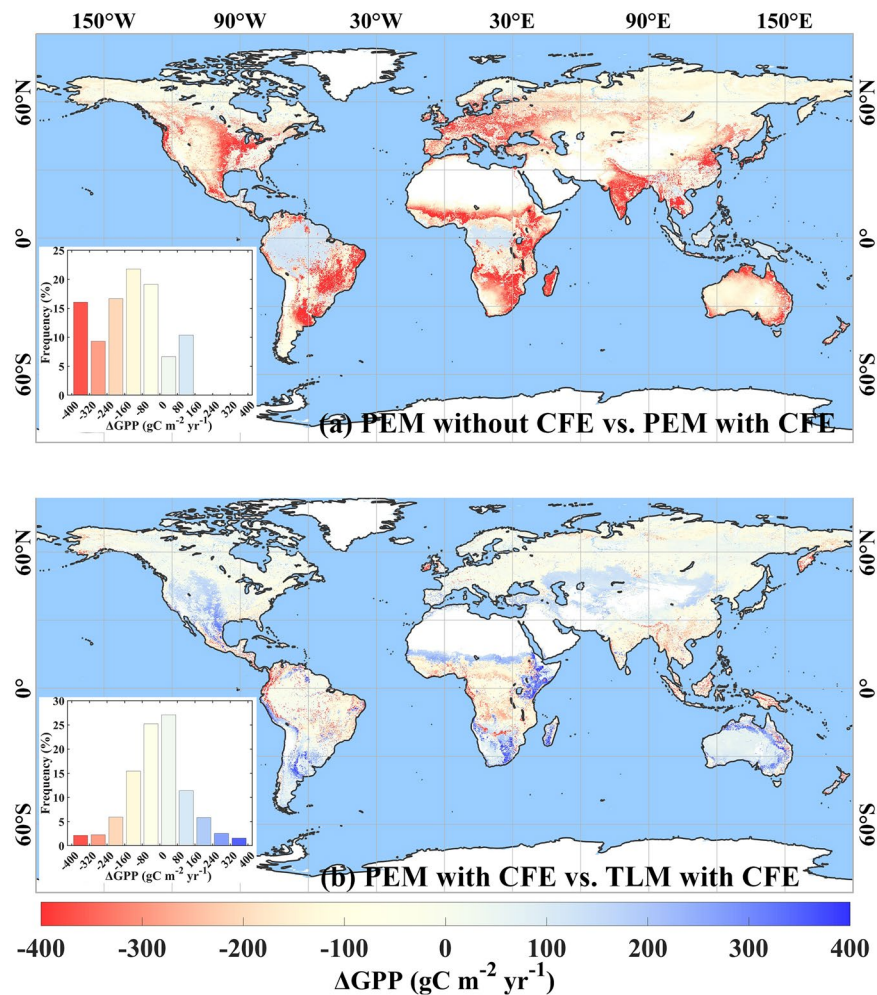
**Fig. 5** Spatial pattern of GPP difference (ΔGPP) for (**a**) 'PEM with CFE' vs. 'PEM without CFE' and (**b**) 'TLM with CFE' vs. 'PEM with CFE'. In panel (**a**), the ΔGPP = GPP$_{\text{PEM without CFE}}$ − GPP$_{\text{PEM with CFE}}$, same for panel (**b**) but the ΔGPP = GPP$_{\text{PEM with CFE}}$ − GPP$_{\text{TLM with CFE}}$. The inset is the histogram of muti-year averaged ΔGPP.

		Mean Annual GPP (Pg C yr^{-1})	Trends in Annual GPP (Pg C yr^{-1} decade^{-1})
PEM	M1C1	132.60 ± 3.22	4.30* (3.25%)
	M2C1	123.23 ± 3.22	3.92* (3.18%)
	M3C1	135.31 ± 5.32	7.59* (5.61%)
	M1C2	130.99 ± 2.69	3.74* (2.85%)
	M2C2	118.84 ± 1.47	1.60* (1.35%)
	M3C2	135.89 ± 4.36	6.24* (4.59%)
TLM	M1C1	133.53 ± 3.30	4.43* (3.32%)
	M2C1	135.12 ± 3.46	4.13* (3.06%)
	M3C1	146.81 ± 6.08	8.64* (5.89%)
	M1C2	131.87 ± 2.76	3.86* (2.93%)
	M2C2	130.37 ± 1.48	1.60* (1.22%)
	M3C2	147.10 ± 5.11	7.32* (4.98%)
RF		138.46 ± 3.43	4.78* (3.58%)
MCI		141.95 ± 4.01	5.70* (5.02%)

Table 1. Mean value of annual GPP and trends in annual GPP from the three PEMs and three TLMs forced with two climate data sets. The three PEMs and three TLMs are denoted as M1, M2, and M3. These models were forced with climate data from GMAO MERRA-2 (C1) and ECMWF ERA-5 (C2). Thus, the notation "M1C1" refers to PEM1 driven with GMAO MERRA-2 climate data.
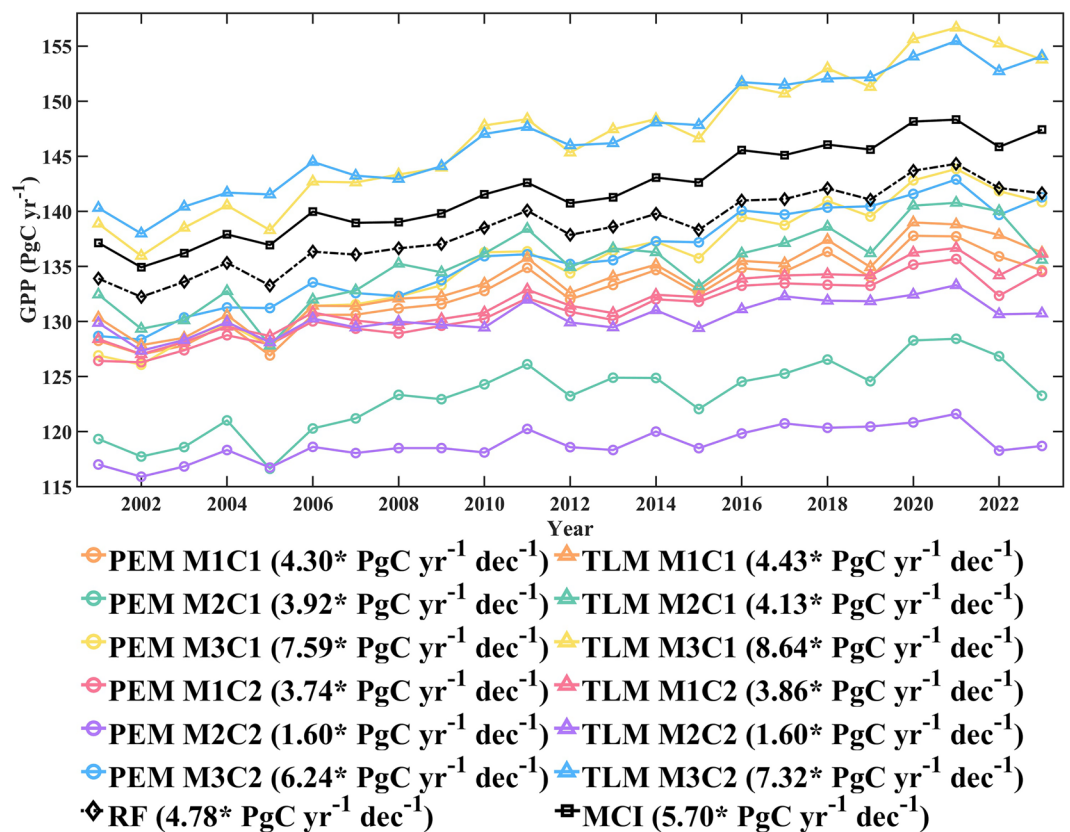
Fig. 6 Dynamic of annual GPPs. These GPPs include RF GPP, MCI GPP, and 12 GPPs from three PEMs and three TLMs, which are forced with two climate data sets. The three PEMs and three TLMs are denoted as M1, M2, and M3. These models were forced with climate data from GMAO MERRA-2 (C1) and ECMWF ERA-5 (C2). Thus, the notation "M1C1" refers to PEM1 driven with GMAO MERRA-2 climate data.

comparable performance, with R^2 values from 0.57 to 0.63 and RMSE values between 2.40 and 2.59 g C m^{-2} d^{-1} (Fig. S4). These performance metrics align with established benchmarks, such as the accuracy of MODIS GPP products, confirming the robustness of both the PEM and TLM frameworks. However, the observed discrepancies among these estimates underscore the potential to enhance global GPP characterization by integrating these diverse model outputs into a more representative and potentially more accurate consolidated product. In addition, both inherent structural flaws in the PEM and TLM models (such as issues with separating sunlit/shaded leaves and light saturation effects) and limitations in the remote sensing input data (specifically the saturation and underestimation of high LAI/FPAR values in dense canopies) collectively lead to the systematic underestimation of GPP when true productivity is high. This significant bias highlights a critical need and large potential for improvement in both canopy photosynthesis modeling and the generation of accurate input data.

After creating 12 PEM/TLM GPPs, the MCI GPP product was integrated using a RF regression algorithm, followed by an ST-Tensor gap-filling method for pixels where the initial 12 GPP uncertainty exceeded 50%. The initial RF GPP estimate yielded a mean annual global GPP of 138.5 ± 3.4 Pg C yr^{-1} across 2001–2023, increasing significantly at a rate of 4.78 Pg C yr^{-1} decade^{-1} (Table 1 and Fig. 6). Subsequently, 17.59% of global pixels (global RI = 82.41%) were filtered and gap-filled by the ST-Tensor method (Fig. 7a). Spatially, over half of all regions (52.95%) consistently maintained high retrieval quality (RI > 90%), primarily concentrated in the Southern Hemisphere and low-latitude Northern Hemisphere. Conversely, only 1.49% of regions required substantial gap-filling (RI < 50%), largely in the mid-to-high latitude Northern Hemisphere, which suggests model disagreement during periods of green-up and senescence. The mean StdGPP for high-quality pixels was 0.73 (Fig. 7b). High StdGPP pixels (StdGPP > 1.4, area = 8.67%) clustered in low-latitude regions (e.g., the Amazon), while low StdGPP pixels (StdGPP < 0.6, area = 41.39%) were common in the high-latitude Northern Hemisphere. Site-scale evaluation of RF GPP and MCI GPP can be found in the 'Site-level evaluation' section and detailed information of MCI GPP can be found in the 'Data Records' section.

Site-level evaluation. The MCI GPP product was developed distinctly for different biome types using monthly FluxNet2015 GPP data and RF regression algorithm. The performance of this training model was assessed by evaluating the intermediate RF-generated GPP estimates against the corresponding FluxNet-derived monthly GPP observations. This evaluation revealed that the RF algorithm explained 82% of the observed monthly GPP variability globally ($R^2 = 0.82$), achieving a RMSE of 1.67 g C m^{-2} d^{-1} and exhibiting minimal systematic bias (Fig. 8a). This also highlights the role of RF algorithms, which nearly eliminate the previous
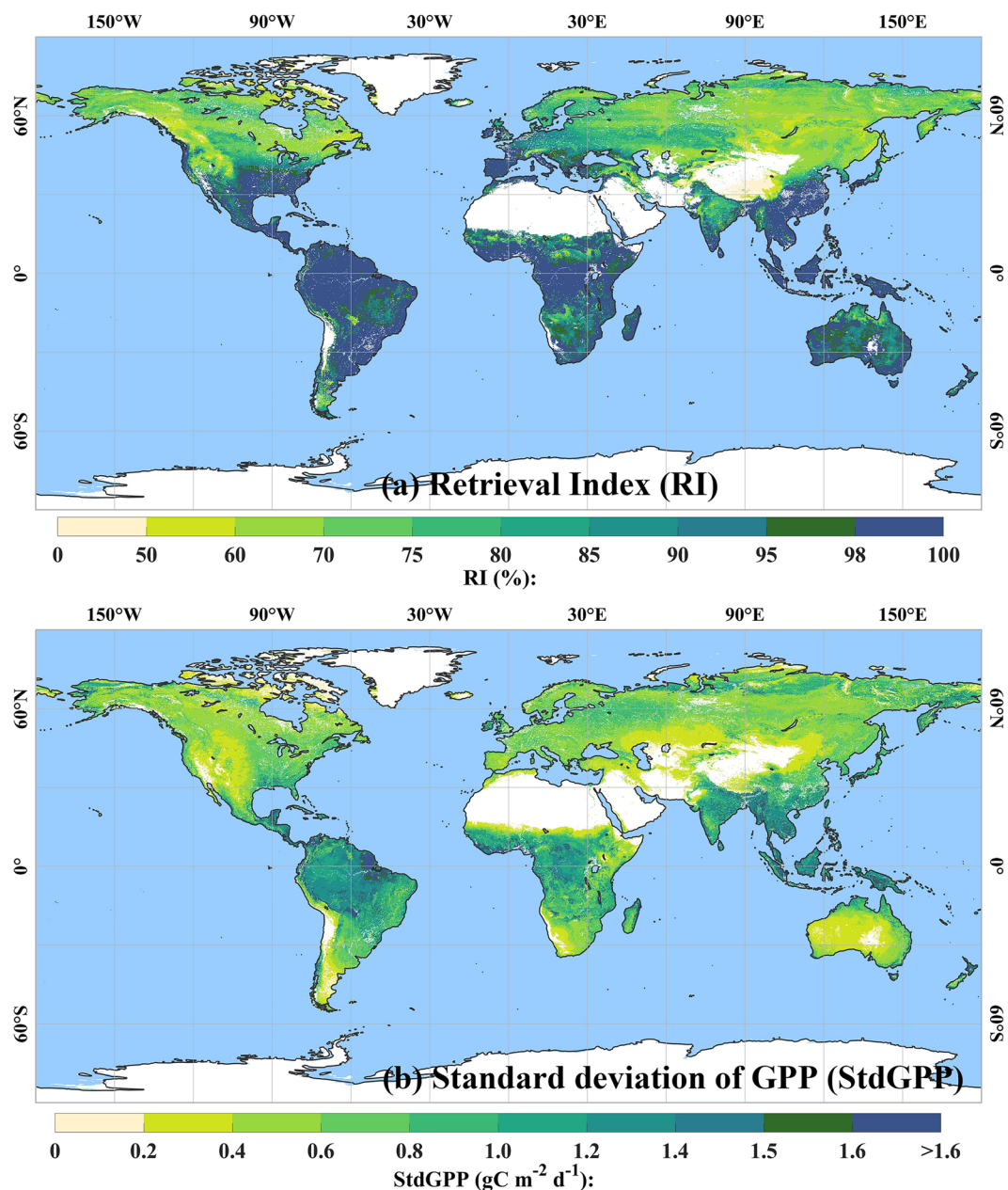
Fig. 7 Spatial pattern of retrieval index (RI, (**a**)) and standard deviation of the 12 GPPs (StdGPP, (**b**)) for MCI GPP from 2001 to 2023.

systematic underestimation by using site data as a reference. The model performed robustly across most biome types: forests, herbaceous vegetation, and other woody vegetation all yielded R^2 values exceeding 0.8 and RMSE values below 1.5 g C m^{-2} d^{-1} (Fig. 8b). Notably, croplands exhibited lower accuracy, with an RMSE of approximately 2.4 g C m^{-2} d^{-1}, indicating systematic discrepancies between the RF model estimates (informed by remote sensing inputs, presumably) and ground observations for this biome. Overall, the strong training accuracy demonstrated by the RF model underscores its reliability in capturing GPP patterns across the majority of evaluated terrestrial ecosystems.

This study compared the performance of MCI GPP and three global GPP products (MOD17, GOSIF, and X-Base Fluxcom) through validation against independent AmeriFlux estimates, which differ from the FluxNet2015 dataset used for model optimization and training. As shown in Fig. 9, the MCI GPP outperformed the other GPPs, achieving an R^2 of 0.72 and an RMSE of 1.86 g C m^{-2} d^{-1}, compared to R^2 values of 0.65~0.71 and RMSE values of 1.93~2.11 g C m^{-2} d^{-1} for MOD17, GOSIF, and X-Base Fluxcom. Biome-specific analysis (Fig. 10) revealed that the MCI GPP demonstrated the highest accuracy for herbaceous and woody vegetation. For forests and croplands, X-Base Fluxcom matched the performance of MCI GPP, though both surpassed MOD17 and GOSIF. Notably, the MCI GPP showed substantial improvement over the individual PEM and TLM
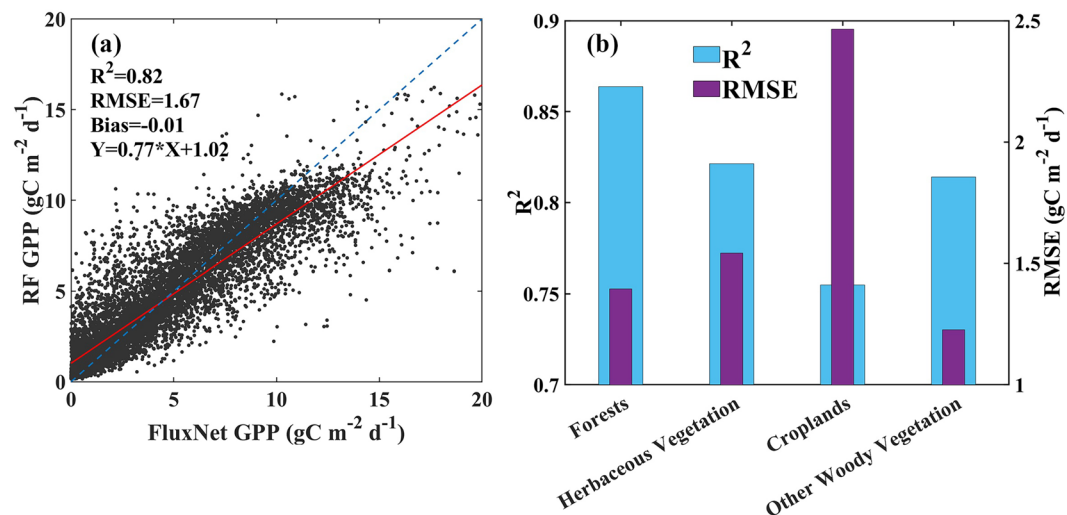
Fig. 8 (**a**) Comparison of annual RF GPP with observations-based GPP from the FluxNet2015. (**b**) The performance of RF GPP against observations-based GPP from the FluxNet2015 for different vegetation types. Forests include ENF, EBF, DNF, DBF, MF. Herbaceous vegetation includes SAV and GRA. Croplands include CRO. Other woody vegetation includes CSH, OSH, and WSA.
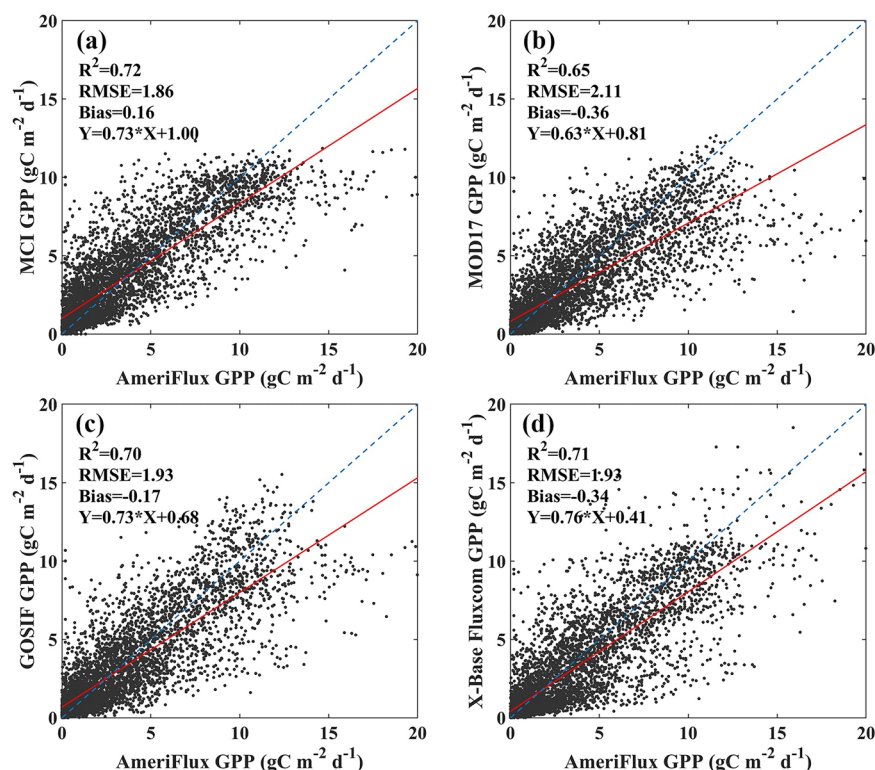
Fig. 9 Comparison of annual GPP from (**a**) MCI, (**b**) MOD17, (**c**) GOSIF, and (**d**) X-Base Fluxcom with observations-based GPP from the AmeriFlux program.

GPPs (Fig. S5), which exhibited similar but lower accuracy. This result underscores the efficacy of the ensemble methodology employed in generating MCI GPP for enhancing the reliability of global GPP estimation.

Global intercomparison with other GPP products. Annual average GPP distributions demonstrate strong concordance between the MCI and GOSIF products (Fig. 11b), with over 81.6% of vegetated areas exhibiting differences below 320 g C m^{-1} d^{-1}. GOSIF GPP further aligns with MCI GPP in decadal growth rates (5.1 Pg C yr^{-1} decade^{-1}) and spatial patterns, where 39.9% of significant greening areas and 5.6% of browning areas coincide (Fig. S6b). In contrast, comparisons with MOD17 and X-Base Fluxcom GPPs (Fig. 11a, c) reveal notable divergence: MCI GPP exhibits higher values across 80.7%–85.8% of vegetated regions. MOD17
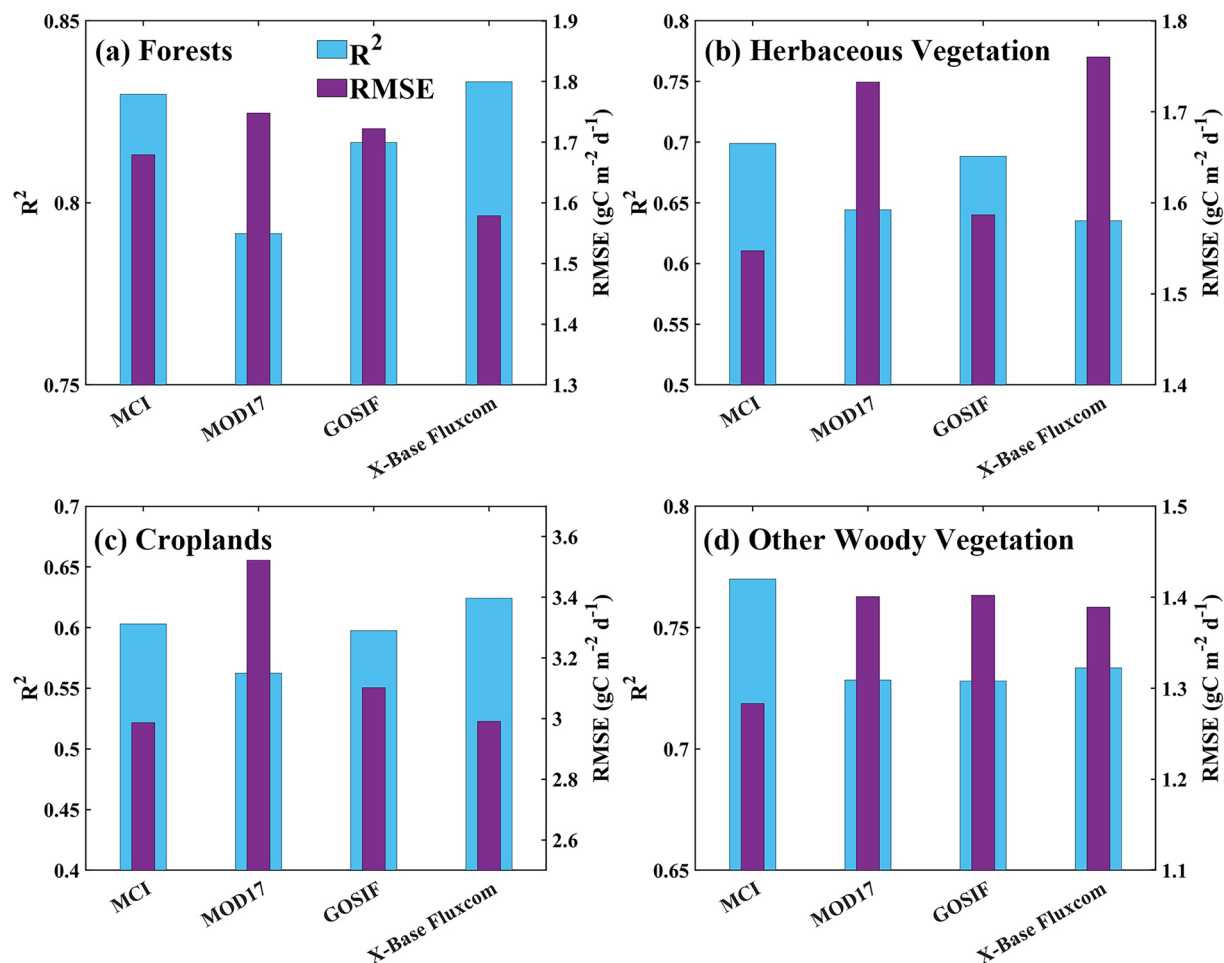
Fig. 10 The performance of (**a**) MCI, (**b**) MOD17, (**c**) GOSIF, and (**d**) X-Base Fluxcom GPPs against observations-based GPP from the AmeriFlux program for different vegetation types. Forests include ENF, EBF, DNF, DBF, MF. Herbaceous vegetation includes SAV and GRA. Croplands include CRO. Other woody vegetation includes CSH, OSH, and WSA.

and X-Base Fluxcom also show weaker decadal growth (2.9 ~ 3.4 Pg C yr^{-1} decade^{-1}) and higher proportions of significantly browning areas (8.1% ~ 8.4%), underscoring differing trend characteristics compared to MCI GPP (Fig. S6a,c).

A newly proposed consistency assessment framework was employed to assess the temporal agreement between the MCI GPP product and three global datasets (MOD17, GOSIF, and X-Base Fluxcom GPPs). Using confidence level testing, monthly GPP variations for each dataset were classified. Confusion matrices were then generated by comparing the classified variations of MCI GPP against those of the other datasets, allowing temporal consistency to be quantified using the OA metric. Results indicated robust alignment between MCI GPP and both MOD17 and X-Base Fluxcom, achieving global OA values of 71.3% and 72.7%, respectively (Fig. 12a,c). In contrast, consistency with GOSIF was comparatively lower (OA = 63.3%). Spatial analysis (Fig. 12b) identified pronounced discrepancies in high-latitude Northern Hemisphere regions, likely stemming from limitations associated with the SIF-GPP relationship underpinning GOSIF. Specifically, potential inaccuracies in SIF retrievals during non-growing seasons and the propagation of errors through non-linear algorithmic components may affect GOSIF GPP estimates. Furthermore, OA exhibited a distinct latitudinal gradient, increasing from the equator towards the poles. This pattern highlights greater uncertainties in tropical GPP estimates, potentially linked to complex vegetation dynamics or sensor/observational limitations in these regions.

Usage Notes

The biophysical mechanisms embedded in LUE models, which simulate vegetation photosynthetic response to climatic forcings (e.g., temperature, water stress, and light availability), have been rigorously evaluated across diverse biomes and spatiotemporal scales[28,30,66]. However, inherent biases within climate reanalysis products propagate directly into LUE-derived GPP estimates, compromising their accuracy. To mitigate this issue, a multi-forcing ensemble approach integrating heterogeneous climate datasets with structurally distinct LUE models has been advocated. This strategy aims to yield a 'bias-resistant' GPP ensemble by decoupling model uncertainties from climate forcing. A critical challenge involves objectively fusing these multi-model, multi-forcing outputs. Conventional static weighting schemes often fail to capture the complex, spatiotemporally
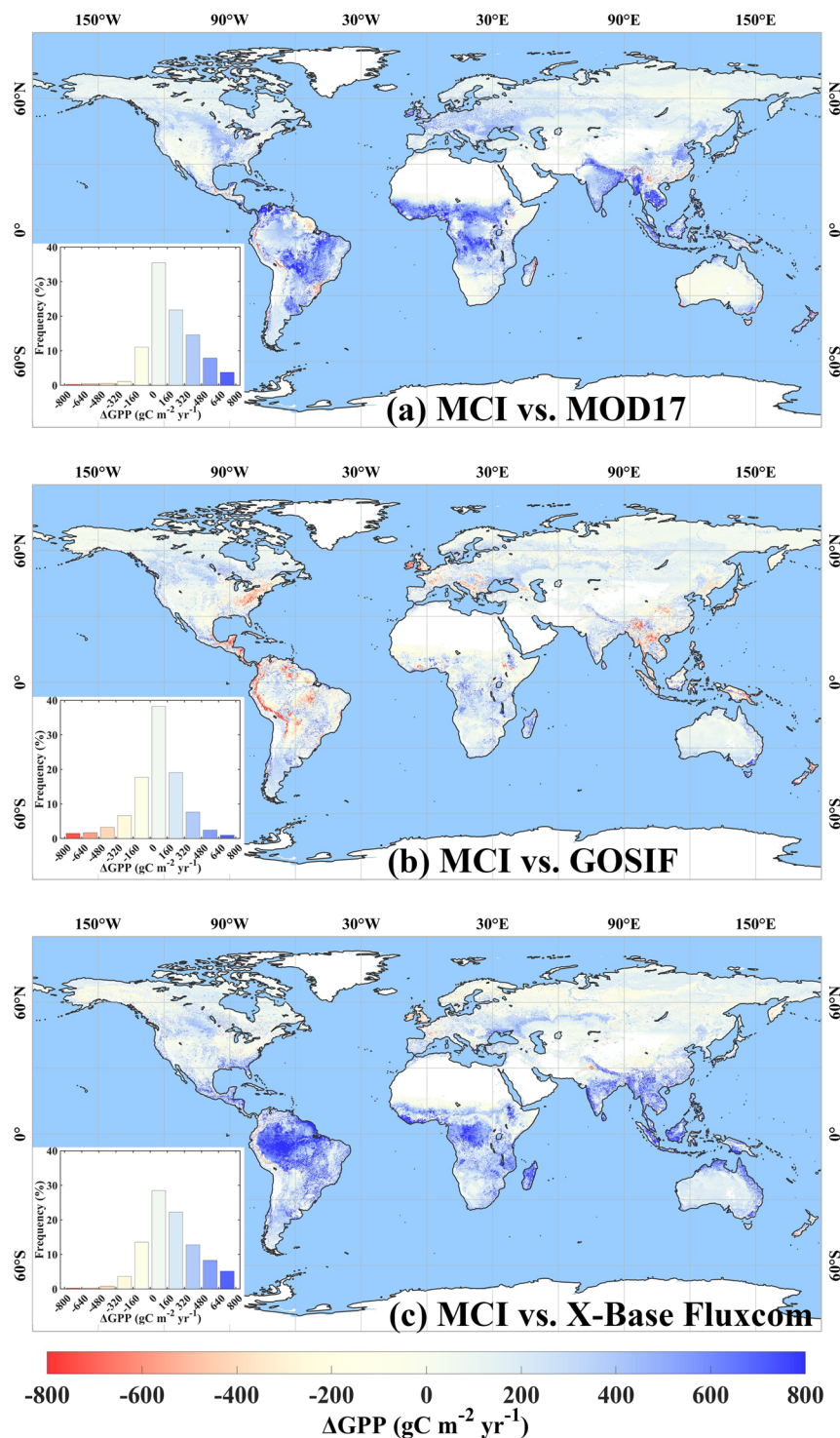
Fig. 11 Spatial pattern of annual averaged GPP difference (ΔGPP) for (**a**) MCI vs. MOD17, (**b**) MCI vs. GOSIF, and (**c**) MCI vs. X-Base Fluxcom from 2001 to 2021. The ΔGPP = GPP$_{MCI}$– GPP$_{MOD17}$, GPP$_{MCI}$– GPP$_{GOSIF}$, and GPP$_{MCI}$– GPP$_{X\text{-}Base\ Fluxcom}$ for panel (**a**), (**b**), and (**c**), respectively. The inset is the histogram of multi-year averaged ΔGPP.

heterogeneous interactions between ecosystem sensitivity and climatic variability. Here, this study harnessed RF as an adaptive weight-modeling tool by training on EC flux tower GPP benchmarks alongside several covariates (model outputs, spatiotemporal information, and land cover), which autonomously derive dynamic weights that reflect ecological realism. Crucially, RF operates strictly as a weight module rather than a primary GPP simulator, thereby preserving the mechanistic transparency of LUE models while circumventing the 'black box' pitfalls for ML methods. During this process, the global annual mean GPP was fixed at approximately 138 Pg
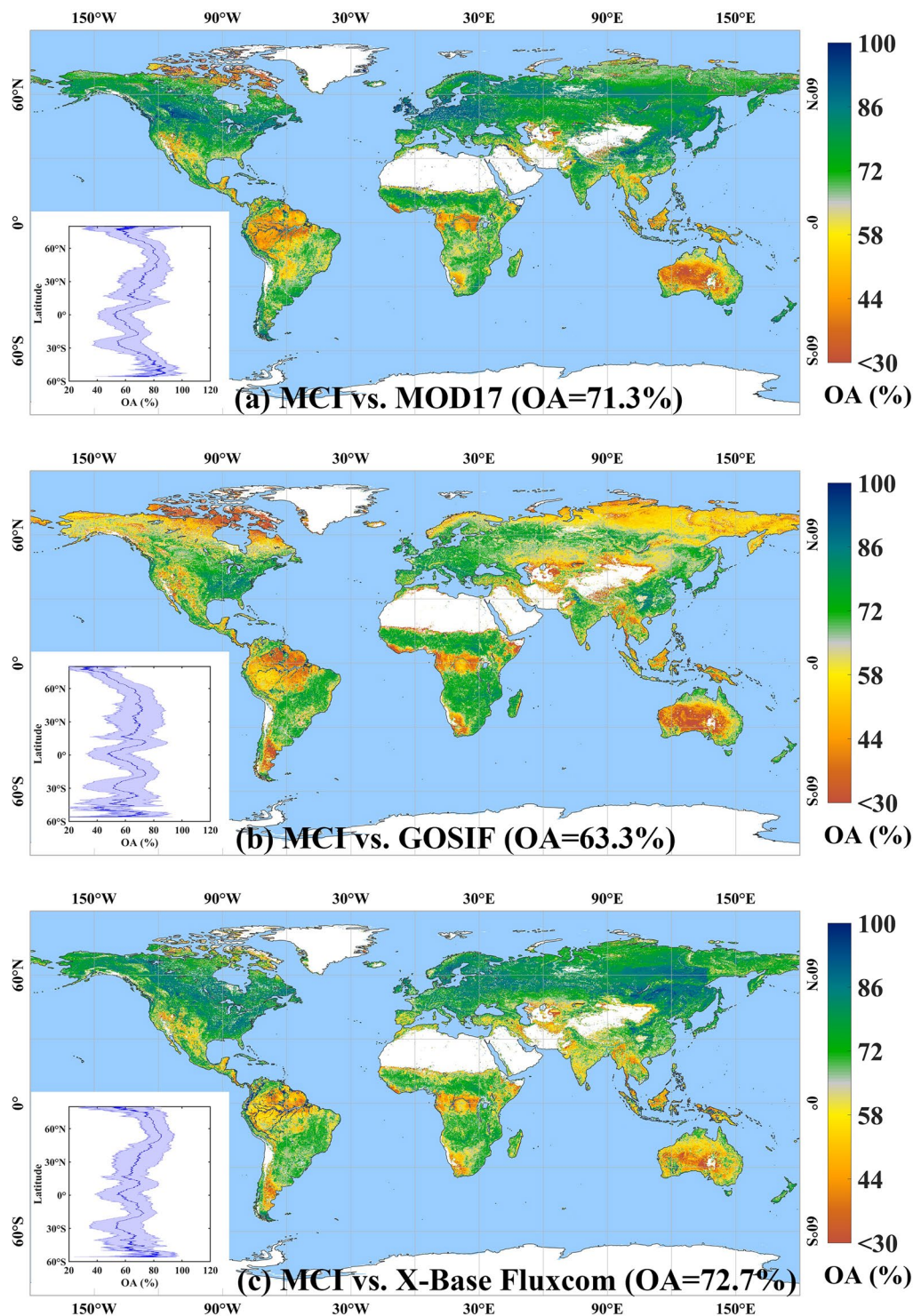
Fig. 12 Spatial pattern of OA for (**a**) MCI vs. MOD17, (**b**) MCI vs. GOSIF, and (**c**) MCI vs. X-Base Fluxcom. Inserting blue lines and shading represent the mean values and standard deviations of GPP OA of the 0.05° latitude zone.

C yr^{-1} from a wide range of values (115 Pg C yr^{-1} to 155 Pg C yr^{-1}, Fig. 6). This estimate aligns with global annual GPP assessments using machine learning algorithms and site-scale GPP as reference data, a finding corroborated by other studies[22,34,39]. To address scenarios where inter-model GPP divergence exceeds ecologically plausible ranges (e.g., conflicting moisture stress parameterizations in semi-arid ecosystems), a backup protocol is implemented. Spatiotemporal gap-filling method will be activated when ensemble variability surpasses a specific threshold, leveraging spatial and temporal patterns to reconstruct outliers, thereby ensuring robustness. Fig. 6 clearly shows that the global annual GPP increased from RF (~138 Pg C yr^{-1}) to MCI (~142 Pg C yr^{-1}).

The premise for gap-filling here is that the standard deviation of the 12 GPPs is greater than 50%, which means that the input data of these pixels in RF regression is not very reliable. We did not directly smooth the GPP time series and did not filter out the disturbance that should exist. Pixels requiring gap-filling are replaced by the GPP after gap-filling and the L1 smooth. The increase in the global GPP annual average from RF GPP to MCI GPP indicates that the RF GPP of pixels that need to be gap-filled is much lower than the RF GPP of the same pixel in the adjacent year and month. This is because the 12 input GPP datasets exhibit large variance, and several are significantly underestimated. This also illustrates the defects of these 12 GPPs and the necessity of gap filling.

In summary, persistent uncertainties in GPP estimation stem from two primary sources: limitations in estimation models and the quality of input data. To overcome these barriers, advancing next-generation GPP frameworks is imperative and should prioritize (1) Mechanistic model advancement: Transitioning from empirical canopy-scale formulations towards leaf-level biochemical models that explicitly resolve photophysics, photobiology, and biochemistry[67–71]. Emerging observational constraints, such as SIF as a proxy for electron transport rates, should be assimilated via data fusion to better constrain model process fidelity. Static parameterizations (e.g., maximum LUE) should evolve into dynamic, phenology-responsive functions modulated by real-time canopy nitrogen content and hydraulic traits[44,72]. (2) Enhanced input data quality: Replacing coarse-resolution climate datasets with high-resolution alternatives and ensuring long-term data continuity (e.g., transitioning from MODIS to VIIRS, maintaining consistent LAI/FPAR records) are crucial for developing reliable, long-term GPP data records like MCI GPP.

Overall, the MCI GPP product developed in this study provides a valuable data asset for investigating long-term vegetation dynamics and ecosystem responses to environmental change. Its potential applications include: 1) re-evaluating regional greening versus browning trends under climate change; 2) tracking phenological changes and differentiating productivity seasonality from canopy greenness signals; 3) constraining global biogeochemical models through data assimilation; 4) assessing ecosystem sensitivity and response to drought; 5) establishing baselines for detecting vegetation stress, especially during extreme weather events; and 6) evaluating vegetation resilience following disturbances such as fire and deforestation.

Data availability
The MCI GPP dataset is available at: https://doi.org/10.5281/zenodo.15204660.

Code availability
The MATLAB code of PEM and TLM GPP generation is openly available at: https://doi.org/10.5281/zenodo.13989451. And we provide MATLAB sample code for processing and using MCI GPP at: https://doi.org/10.5281/zenodo.15204660.

References
1. Friedlingstein, P. *et al*. Global Carbon Budget 2023. *Earth Syst. Sci. Data* **15**, 5301–5369, https://doi.org/10.5194/essd-15-5301-2023 (2023).
2. Sellers, P. J., Schimel, D. S., Moore, B., Liu, J. & Eldering, A. Observing carbon cycle–climate feedbacks from space. *Proceedings of the National Academy of Sciences* **115**, 7860–7868, https://doi.org/10.1073/pnas.1716613115 (2018).
3. Prentice, I. C. *et al*. Principles for satellite monitoring of vegetation carbon uptake. *Nature Reviews Earth & Environment* **5**, 818–832, https://doi.org/10.1038/s43017-024-00601-6 (2024).
4. Chen, C., Riley, W. J., Prentice, I. C. & Keenan, T. F. CO2 fertilization of terrestrial photosynthesis inferred from site to global scales. *Proceedings of the National Academy of Sciences* **119**, e2115627119, https://doi.org/10.1073/pnas.2115627119 (2022).
5. Keenan, T. F. *et al*. A constraint on historic growth in global photosynthesis due to rising CO2. *Nature Climate Change* **13**, 1376–1381, https://doi.org/10.1038/s41558-023-01867-2 (2023).
6. Ruehr, S. *et al*. Evidence and attribution of the enhanced land carbon sink. *Nature Reviews Earth & Environment* **4**, 518–534, https://doi.org/10.1038/s43017-023-00456-3 (2023).
7. Field, C. B., Behrenfeld, M. J., Randerson, J. T. & Falkowski, P. Primary Production of the Biosphere: Integrating Terrestrial and Oceanic Components. *Science* **281**, 237–240, https://doi.org/10.1126/science.281.5374.237 (1998).
8. Beer, C. *et al*. Terrestrial Gross Carbon Dioxide Uptake: Global Distribution and Covariation with Climate. *Science* **329**, 834–838, https://doi.org/10.1126/science.1184984 (2010).
9. Welp, L. R. *et al*. Interannual variability in the oxygen isotopes of atmospheric CO2 driven by El Niño. *Nature* **477**, 579–582, https://doi.org/10.1038/nature10421 (2011).
10. Anav, A. *et al*. Spatiotemporal patterns of terrestrial gross primary production: A review. *Reviews of Geophysics* **53**, 785–818, https://doi.org/10.1002/2015RG000483 (2015).
11. Ryu, Y., Berry, J. A. & Baldocchi, D. D. What is global photosynthesis? History, uncertainties and opportunities. *Remote Sensing of Environment* **223**, 95–114, https://doi.org/10.1016/j.rse.2019.01.016 (2019).
12. Yuan, W. *et al*. Global estimates of evapotranspiration and gross primary production based on MODIS and global meteorology data. *Remote Sensing of Environment* **114**, 1416–1431, https://doi.org/10.1016/j.rse.2010.01.022 (2010).
13. Jung, M. *et al*. Scaling carbon fluxes from eddy covariance sites to globe: synthesis and evaluation of the FLUXCOM approach. *Biogeosciences* **17**, 1343–1365, https://doi.org/10.5194/bg-17-1343-2020 (2020).
14. Zhu, W. *et al*. Remote sensing of terrestrial gross primary productivity: a review of advances in theoretical foundation, key parameters and methods. *GIScience & Remote Sensing* **61**, 2318846, https://doi.org/10.1080/15481603.2024.2318846 (2024).
15. Baldocchi, D. Assessing the eddy covariance technique for evaluating carbon dioxide exchange rates of ecosystems: past, present and future. *Global Change Biology* **9**, 479–492, https://doi.org/10.1046/j.1365-2486.2003.00629.x (2003).
16. Baldocchi, D., Chu, H. & Reichstein, M. Inter-annual variability of net and gross ecosystem carbon fluxes: A review. *Agricultural and Forest Meteorology* **249**, 520–533, https://doi.org/10.1016/j.agrformet.2017.05.015 (2018).
17. Pastorello, G. *et al*. The FLUXNET2015 dataset and the ONEFlux processing pipeline for eddy covariance data. *Scientific Data* **7**, 225, https://doi.org/10.1038/s41597-020-0534-3 (2020).
18. Nelson, J. A. *et al*. X-BASE: the first terrestrial carbon and water flux products from an extended data-driven scaling framework, FLUXCOM-X. *Biogeosciences* **21**, 5079–5115, https://doi.org/10.5194/bg-21-5079-2024 (2024).
19. Chen, X. *et al*. A 2001–2022 global gross primary productivity dataset using an ensemble model based on the random forest method. *Biogeosciences* **21**, 4285–4300, https://doi.org/10.5194/bg-21-4285-2024 (2024).

20. Wang, T. *et al.* Progress and challenges in remotely sensed terrestrial carbon fluxes. *Geo-spatial Information Science*, 1–21, https://doi.org/10.1080/10095020.2024.2336599 (2024).
21. O'Sullivan, M. *et al.* Climate-Driven Variability and Trends in Plant Productivity Over Recent Decades Based on Three Global Products. *Global Biogeochemical Cycles* **34**, e2020GB006613, https://doi.org/10.1029/2020GB006613 (2020).
22. Li, X. & Xiao, J. Mapping Photosynthesis Solely from Solar-Induced Chlorophyll Fluorescence: A Global, Fine-Resolution Dataset of Gross Primary Production Derived from OCO-2. *Remote Sensing* **11**, 2563, https://doi.org/10.3390/rs11212563 (2019).
23. Bai, J. *et al.* Estimation of global GPP from GOME-2 and OCO-2 SIF by considering the dynamic variations of GPP-SIF relationship. *Agricultural and Forest Meteorology* **326**, 109180, https://doi.org/10.1016/j.agrformet.2022.109180 (2022).
24. Monteith, J. L. Solar Radiation and Productivity in Tropical Ecosystems. *Journal of Applied Ecology* **9**, 747–766, https://doi.org/10.2307/2401901 (1972).
25. Running, S. W. *et al.* A continuous satellite-derived measure of global terrestrial primary production. *Bioscience* **54**, 1525–3244, https://doi.org/10.1641/0006-3568(2004)054[0547:ACSMOG]2.0.CO;2 (2004).
26. Endsley, K. A., Zhao, M., Kimball, J. S. & Devadiga, S. Continuity of global MODIS terrestrial primary productivity estimates in the VIIRS era using model-data fusion. *Journal of Geophysical Research: Biogeosciences*, e2023JG007457, https://doi.org/10.1029/2023JG007457 (2023).
27. Román, M. O. *et al.* Continuity between NASA MODIS Collection 6.1 and VIIRS Collection 2 land products. *Remote Sensing of Environment* **302**, 113963, https://doi.org/10.1016/j.rse.2023.113963 (2024).
28. Yuan, W. *et al.* Deriving a light use efficiency model from eddy covariance flux data for predicting daily gross primary production across biomes. *Agricultural and Forest Meteorology* **143**, 189–207, https://doi.org/10.1016/j.agrformet.2006.12.001 (2007).
29. Yuan, W. *et al.* Increased atmospheric vapor pressure deficit reduces global vegetation growth. *Science Advances* **5**, eaax1396, https://doi.org/10.1126/sciadv.aax1396 (2019).
30. Xiao, X. *et al.* Satellite-based modeling of gross primary production in an evergreen needleleaf forest. *Remote Sensing of Environment* **89**, 519–534, https://doi.org/10.1016/j.rse.2003.11.008 (2004).
31. Farquhar, G. D., von Caemmerer, S. V. & Berry, J. A. A biochemical model of photosynthetic CO_2 assimilation in leaves of C3 species. *planta* **149**, 78–90, https://doi.org/10.1007/BF00386231 (1980).
32. Stocker, B. D. *et al.* P-model v1.0: an optimality-based light use efficiency model for simulating ecosystem gross primary production. *Geosci. Model Dev.* **13**, 1545–1581, https://doi.org/10.5194/gmd-13-1545-2020 (2020).
33. Li, B. *et al.* BESSv2.0: A satellite-based and coupled-process model for quantifying long-term global land–atmosphere fluxes. *Remote Sensing of Environment* **295**, 113696, https://doi.org/10.1016/j.rse.2023.113696 (2023).
34. Leng, J. *et al.* Global datasets of hourly carbon and water fluxes simulated using a satellite-based process model with dynamic parameterizations. *Earth Syst. Sci. Data* **16**, 1283–1300, https://doi.org/10.5194/essd-16-1283-2024 (2024).
35. Huang, X. *et al.* High spatial resolution vegetation gross primary production product: Algorithm and validation. *Science of Remote Sensing* **5**, 100049, https://doi.org/10.1016/j.srs.2022.100049 (2022).
36. Keenan, T. F. *et al.* Recent pause in the growth rate of atmospheric CO_2 due to enhanced terrestrial carbon uptake. *Nature Communications* **7**, 13428, https://doi.org/10.1038/ncomms13428 (2016).
37. Fatichi, S. *et al.* Partitioning direct and indirect effects reveals the response of water-limited ecosystems to elevated CO_2. *Proceedings of the National Academy of Sciences* **113**, 12757–12762, https://doi.org/10.1073/pnas.1605036113 (2016).
38. Wang, H. *et al.* Towards a universal model for carbon dioxide uptake by plants. *Nature plants* **3**, 734–741, https://doi.org/10.1038/s41477-017-0006-8 (2017).
39. Kang, Y., Bassiouni, M., Gaber, M., Lu, X. & Keenan, T. F. CEDAR-GPP: spatiotemporally upscaled estimates of gross primary productivity incorporating CO_2 fertilization. *Earth Syst. Sci. Data* **17**, 3009–3046, https://doi.org/10.5194/essd-17-3009-2025 (2025).
40. He, M. *et al.* Development of a two-leaf light use efficiency model for improving the calculation of terrestrial gross primary productivity. *Agricultural and Forest Meteorology* **173**, 28–39, https://doi.org/10.1016/j.agrformet.2013.01.003 (2013).
41. Thornley, J. H. M. Instantaneous Canopy Photosynthesis: Analytical Expressions for Sun and Shade Leaves Based on Exponential Light Decay Down the Canopy and an Acclimated Non-rectangular Hyperbola for Leaf Photosynthesis. *Annals of Botany* **89**, 451–458, https://doi.org/10.1093/aob/mcf071 (2002).
42. Xu, H., Zhang, Z., Wu, X. & Wan, J. Light use efficiency models incorporating diffuse radiation impacts for simulating terrestrial ecosystem gross primary productivity: A global comparison. *Agricultural and Forest Meteorology* **332**, 109376, https://doi.org/10.1016/j.agrformet.2023.109376 (2023).
43. Bao, S. *et al.* Environment-sensitivity functions for gross primary productivity in light use efficiency models. *Agricultural and Forest Meteorology* **312**, 108708, https://doi.org/10.1016/j.agrformet.2021.108708 (2022).
44. Huang, L. *et al.* A dynamic-leaf light use efficiency model for improving gross primary production estimation. *Environmental Research Letters* **19**, 014066, https://doi.org/10.1088/1748-9326/ad1726 (2024).
45. Li, X., Liang, H. & Cheng, W. Evaluation and comparison of light use efficiency models for their sensitivity to the diffuse PAR fraction and aerosol loading in China. *International Journal of Applied Earth Observation and Geoinformation* **95**, 102269, https://doi.org/10.1016/j.jag.2020.102269 (2021).
46. Zheng, Y. *et al.* Improved estimate of global gross primary production for reproducing its long-term variation, 1982–2017. *Earth Syst. Sci. Data* **12**, 2725–2746, https://doi.org/10.5194/essd-12-2725-2020 (2020).
47. Buck, A. L. New Equations for Computing Vapor Pressure and Enhancement Factor. *Journal of Applied Meteorology and Climatology* **20**, 1527–1532, 10.1175/1520-0450(1981)020<1527:NEFCVP>2.0.CO;2 (1981).
48. Pu, J. *et al.* Sensor-independent LAI/FPAR CDR: reconstructing a global sensor-independent climate data record of MODIS and VIIRS LAI/FPAR from 2000 to 2022. *Earth Syst. Sci. Data* **16**, 15–34, https://doi.org/10.5194/essd-16-15-2024 (2024).
49. Lobell, D. B. & Field, C. B. Estimation of the carbon dioxide (CO_2) fertilization effect using growth rate anomalies of CO_2 and crop yields since 1961. *Global Change Biology* **14**, 39–45, https://doi.org/10.1111/j.1365-2486.2007.01476.x (2008).
50. Sulla-Menashe, D. & Friedl, M. A. User Guide to Collection 6 MODIS Land Cover (MCD12Q1 and MCD12C1) Product. http://girps.net/wp-content/uploads/2019/03/MCD12_User_Guide_V6.pdf (2018).
51. Novick, K. A. *et al.* The AmeriFlux network: A coalition of the willing. *Agricultural and Forest Meteorology* **249**, 444–456, https://doi.org/10.1016/j.agrformet.2017.10.009 (2018).
52. Bao, S. *et al.* Narrow but robust advantages in two-big-leaf light use efficiency models over big-leaf light use efficiency models at ecosystem level. *Agricultural and Forest Meteorology* **326**, 109185, https://doi.org/10.1016/j.agrformet.2022.109185 (2022).
53. Kalliokoski, T., Mäkelä, A., Fronzek, S., Minunno, F. & Peltoniemi, M. Decomposing sources of uncertainty in climate change projections of boreal forest primary production. *Agricultural and Forest Meteorology* **262**, 192–205, https://doi.org/10.1016/j.agrformet.2018.06.030 (2018).
54. Chen, Y., Yuan, H., Yang, Y. & Sun, R. Sub-daily soil moisture estimate using dynamic Bayesian model averaging. *Journal of Hydrology* **590**, 125445, https://doi.org/10.1016/j.jhydrol.2020.125445 (2020).
55. Tian, Z. *et al.* Fusion of Multiple Models for Improving Gross Primary Production Estimation With Eddy Covariance Data Based on Machine Learning. *Journal of Geophysical Research: Biogeosciences* **128**, e2022JG007122, https://doi.org/10.1029/2022JG007122 (2023).
56. Zhang, H., Liu, L., He, W. & Zhang, L. Hyperspectral image denoising with total variation regularization and nonlocal low-rank tensor decomposition. *IEEE Transactions on Geoscience and Remote Sensing* **58**, 3071–3084, https://doi.org/10.1109/TGRS.2019.2947333 (2019).

57. Chu, D. *et al.* Long time-series NDVI reconstruction in cloud-prone regions via spatio-temporal tensor completion. *Remote Sensing of Environment* **264**, 112632, https://doi.org/10.1016/j.rse.2021.112632 (2021).

58. Ji, T.-Y., Huang, T.-Z., Zhao, X.-L., Ma, T.-H. & Deng, L.-J. A non-convex tensor rank approximation for tensor completion. *Applied Mathematical Modelling* **48**, 410–422, https://doi.org/10.1016/j.apm.2017.04.002 (2017).

59. Ji, T.-Y., Yokoya, N., Zhu, X. X. & Huang, T.-Z. Nonlocal tensor completion for multitemporal remotely sensed images' inpainting. *IEEE Transactions on Geoscience and Remote Sensing* **56**, 3047–3061, https://doi.org/10.1109/TGRS.2018.2790262 (2018).

60. Chu, D., Shen, H., Guan, X. & Li, X. An L1-regularized variational approach for NDVI time-series reconstruction considering inter-annual seasonal similarity. *International Journal of Applied Earth Observation and Geoinformation* **114**, 103021, https://doi.org/10.1016/j.jag.2022.103021 (2022).

61. Mota, B. *et al.* Cross-ECV consistency at global scale: LAI and FAPAR changes. *Remote Sensing of Environment* **263**, 112561, https://doi.org/10.1016/j.rse.2021.112561 (2021).

62. Hamed, K. H. & Rao, A. R. A modified Mann-Kendall trend test for autocorrelated data. *Journal of hydrology* **204**, 182–196, https://doi.org/10.1016/S0022-1694(97)00125-X (1998).

63. Pu, J., Chang, Y. & Myneni, R. MCI GPP: ensembling a global model- and climate-independent gross primary productivity for 2001–2023. *Zenodo* https://doi.org/10.5281/zenodo.15204660 (2025).

64. Piao, S. *et al.* Characteristics, drivers and feedbacks of global greening. *Nature Reviews Earth & Environment* **1**, 14–27, https://doi.org/10.1038/nclimate3004 (2020).

65. Zhu, Z. *et al.* Greening of the Earth and its drivers. *Nature Climate Change* **6**, 791–795, https://doi.org/10.1038/nclimate3004 (2016).

66. Sánchez, M., Pardo, N., Pérez, I. & García, M. GPP and maximum light use efficiency estimates using different approaches over a rotating biodiesel crop. *Agricultural and Forest Meteorology* **214**, 444–455, https://doi.org/10.1016/j.agrformet.2015.09.012 (2015).

67. Bacour, C. *et al.* Improving Estimates of Gross Primary Productivity by Assimilating Solar-Induced Fluorescence Satellite Retrievals in a Terrestrial Biosphere Model Using a Process-Based SIF Model. *Journal of Geophysical Research: Biogeosciences* **124**, 3281–3306, https://doi.org/10.1029/2019JG005040 (2019).

68. Liu, Z. *et al.* A SIF-based approach for quantifying canopy photosynthesis by simulating the fraction of open PSII reaction centers (qL). *Remote Sensing of Environment* **305**, 114111, https://doi.org/10.1016/j.rse.2024.114111 (2024).

69. Guo, C., Liu, Z., Jin, X. & Lu, X. Improved estimation of gross primary productivity (GPP) using solar-induced chlorophyll fluorescence (SIF) from photosystem II. *Agricultural and Forest Meteorology* **354**, 110090, https://doi.org/10.1016/j.agrformet.2024.110090 (2024).

70. Chen, R. *et al.* SIF-based GPP modeling for evergreen forests considering the seasonal variation in maximum photochemical efficiency. *Agricultural and Forest Meteorology* **344**, 109814, https://doi.org/10.1016/j.agrformet.2024.110090 (2024).

71. Fang, J. *et al.* A long-term reconstruction of a global photosynthesis proxy over 1982–2023. *Scientific Data* **12**, 372, https://doi.org/10.1038/s41597-025-04686-6 (2025).

72. Bao, S. *et al.* Toward Robust Parameterizations in Ecosystem-Level Photosynthesis Models. *Journal of Advances in Modeling Earth Systems* **15**, e2022MS003464, https://doi.org/10.1029/2022MS003464 (2023).

Acknowledgements

Author contributions

JP: Conceptualization, Data curation, Formal analysis, Investigation, Methodology, Software, Validation, Visualization, Writing – original draft. YC: Conceptualization, Data curation, Formal analysis, Methodology, Validation. SG: Formal analysis, Investigation, Validation, Writing – review & editing. SB: Formal analysis, Methodology, Software, Writing – review & editing. KY: Investigation, Methodology, Supervision. Writing – review & editing. XS: Formal analysis, Supervision. NC: Conceptualization, Methodology, Resources. RM: Conceptualization, Funding acquisition, Methodology, Project administration, Resources, Supervision.

Competing interests

The authors declare that they have no known competing financial interests or personal relationships that could have influenced the work reported in this study.

Additional information

Supplementary information The online version contains supplementary material available at https://doi.org/10.1038/s41597-025-06218-8.

Correspondence and requests for materials should be addressed to K.Y.

Reprints and permissions information is available at www.nature.com/reprints.

Publisher's note Springer Nature remains neutral with regard to jurisdictional claims in published maps and institutional affiliations.